Estimation of the relative contributions to the electronic energy transfer rates based on Förster theory: The case of C-phycocyanin chromophores

Kenji Mishima, Mitsuo Shoji, Yasufumi Umena, Mauro Boero, Yasuteru Shigeta

Estimation of the relative contributions to the electronic energy transfer rates based on Förster theory: The case of C-phycocyanin chromophores

Kenji Mishima,*[1] Mitsuo Shoji,*[1,2] Yasufumi Umena,[3] Mauro Boero,[4] and Yasuteru Shigeta[1]

[1]Center for Computational Sciences, University of Tsukuba, 1-1-1 Tennodai, Tsukuba, Ibaraki 305-8577, Japan

[2]JST-PRESTO, 4-1-8 Honcho, Kawaguchi, Saitama, 332-0012, Japan

[3] Department of Physiology, Division of Biophysics, Jichi Medical University, 3311-1 Yakushiji, Shimotsuke, Tochigi 329-0498, Japan

[4]University of Strasbourg, Institut de Physique et Chimie des Matériaux de Strasbourg, CNRS, UMR 7504, 23 rue du Loess, F-67034 France

E-mail: mishima.kenji.fu@u.tsukuba.ac.jp (K. Mishima), mshoji@ccs.tsukuba.ac.jp (M. Shoji)

Abstract

In the present study, we provide a reformulation of the theory originally proposed by Förster which allows for simple and convenient formulas useful to estimate the relative contributions of transition dipole moments of a donor and acceptor (chemical factors), their orientation factors (intermolecular structural factors), intermolecular center-to-center distances (intermolecular structural factors), spectral overlaps of absorption and emission spectra (photophysical factors), and refractive index (material factor) to the excitation energy transfer (EET) rate constant. To benchmark their validity, we focused on the EET occurring in C-phycocyanin (C-PC) chromophores. To this aim, we resorted to quantum chemistry calculations to get optimized molecular structures of the C-PC chromophores within the density functional theory (DFT) framework. The absorption and emission spectra, as well as transition dipole moments, were computed by using the time-dependent DFT (TDDFT). Our method was applied to several types of C-PCs showing that the EET rates are determined by an interplay of their specific physical, chemical, and geometrical features. These results show that our formulas can become a useful tool for a reliable estimation of the relative contributions of the factors regulating the EET transfer rate.

Keywords: photosynthesis, quantum chemistry calculations, transition dipole moments, absorption and emission spectra, intermolecular center-to-center distance

1. Introduction

Photosynthesis is the key mechanism responsible for the conversion of sunlight into energy and this energy is exploited by both terrestrial plants and algae. Phycobiliproteins (PBPs) are pigment proteins which play a pivotal role in photosynthesis as the light-harvesting components in cyanobacteria and red algae [1]. PBPs are water-soluble and, at variance with carotenoids, cannot exist within the membrane. As a consequence, they assemble into clusters which adhere to the membrane and are generally referred to as phycobilisomes. PBPs are heterodimers composed of α and β subunits, each of which possesses one to three open-chain covalently attached tetrapyrrole or phycobilins via thioether bonds to the apoprotein [2-4]. Another important role of PBPs is to convey the light energy to chlorophylls and finally to the photochemical reaction center for photosynthesis [5,6].

Phycobilins act as chromophores, the light-capturing moiety in photosynthesis. Major phycobilins include R-phycoerythrin (R-PE), B-phycoerythrin (B-PE), C-phycocyanin (C-PC), and

allophycocyanin (APC) [7-9]. Their photophysical features, and in particular the absorption and fluorescence spectra, have been extensively investigated [10-22]. The common photophysical features of phycobilins can be summarized into one high absorption in the Q-band at around 700 nm and a large number of small absorption peaks in the Soret band at around 400 nm. They are typically classified in terms of their spectral features; R-PE and B-PE with λ_{max}=540-570 nm, C-PC with λ_{max}=610-620 nm, and APC with λ_{max}=650-655 nm, where λ_{max} is the wavelength of the band maximum in the Q-band [23, 24]. These differences are known to be induced by different π-conjugation lengths in the tetrapyrrole rings [25]. In addition, because of their similarities in structure and function, it is assumed that they have a common ancestral gene [26].

Although the crystal structures of the PBPs have been intensively investigated over the years using X-rays, it is still difficult nowadays to unravel, for instance, how many phycobilins a given PBP contains. The C-PC system, targeted in the present study, is a peculiar phycocyanin which contains only phycocyanobilin chromophores. C-PC is composed of two homologous subunits; the α-chain with one phycocyanobilin attached at cysteine 84 and the β-chain with two phycocyanobilins attached at cysteines 84 and 155 [27-30]. These two homologous subunits form αβ monomers, aggregate into $(\alpha\beta)_3$ trimers, and furthermore into disc-shaped $(\alpha\beta)_6$ hexamers, the functional unit of C-PC.

Historically, Schirmer and coworkers determined the crystal structure of the biliprotein C-PC from the thermophilic cyanobacterium *Mastigocladus laminosus* by X-ray diffraction with a resolution of 3Å for the first time [31]. In that work, it was found that the protein consists of three identical (αβ)-units which are arranged around a threefold symmetry axis to form a disc of the approximate dimensions of 110 Å × 30 Å with a central channel of 35 Å diameter. This aggregation form was supposed to be identical to the one found in the rods of native phycobilisomes. To date, these findings are the most important structural features reported for C-PC.

Subsequent accurate X-ray structural studies of C-PC from a variety of organisms were reported. In general, almost all these studies have shown that the overall sequences of the C-PC complexes are very similar, albeit slight differences in their biophysical and biochemical properties [28-30, 32-45].

Nield and coworkers reported a 1.45 Å resolution for the three-dimensional structure of C-PC from *Synechococcus elongatus* [33], which was the best possible resolution at the date of the publication of that work. They found that C-PCs are covalently bound to the protein via cysteines α-84, β-84, and β-155. The positions of α-84 and β-84 are similar to those of the heme-binding sites of myoglobin, with the thioether bonds in the R stereo-isomer conformation. The β-155 binding site is located in a short insertion loop not found in the α subunit. Its thioether bond has a typical S stereo-isomer conformation. All three pyrrole tetrapyrrole rings show a Z configuration on the D ring. The structures are analogous to those of the *Cyanidium caldarium* [28]. The difference stems from the different packing arrangement at the interface between the trimers, arising from the lack of conservation of the amino acid sequences [29].

Concerning the functional properties of PBP, crucial factors determining the efficiency of photosynthesis are the efficient collection of sunlight suitable for exciting the reaction centers of the system and, consequently, to transfer these excitation energies toward the photosynthetic pigment antennas. This process is termed electron energy transfer (EET) [46]. The EET process consists of the absorption of light by one pigment and the transfer of the resulting excitation energy to one or more other pigments. Phycobilisomes are efficient energy transducers, transferring the absorbed light to the photosystem II with an efficiency greater than 95% [47,48].

Several investigations of the EET in C-phycocyanin [30,49-64], done with picosecond fluorescence measurements, have shown that EET occurs from high (sensitizing) to low (fluorescing) energy phycobilins on isolated phycocyanin aggregates, which are fast components (10-80 ps), accompanied by a much longer decay of ~ 1-2 ns, corresponding to the normal radiative emission from the fluorescing chromophores.

From a theoretical standpoint, the EET among weakly coupled pigments was originally formulated by Thomas Förster [65,66]. The Förster theory has often been applied to the interpretations of the experimental results, proving its versatility and reliability [67]. Since the original formulation of the Förster theory, several developments have been proposed and the EET rate constants have been calculated using these new sophisticated formulations [68-76].

Although it is currently possible to quantitatively estimate the EET rate constant, it is not necessarily clear which physical and chemical factors contribute to it and to which extent. Thus, despite being quantitatively accurate, it remains difficult to extract a precise microscopic picture suitable, for instance, to unravel at a molecular level, the experimental investigation aimed at controlling the energy transfer dynamics of a Förster resonance energy transfer (FRET) for a coupled pair of chromophores embedded in a tunable sub-wavelength Fabry-Pérot resonator [77] or for enhancing the FRET rate in several FRET-based applications [78]. Regarding the specific context of photosynthesis, a variety of EET theoretical formulations have been applied to study this process in pigments, and this is the case of C-PCs [79-83]. The attention received by this specific system worldwide stems from the fact that C-PC pigments are the major phycobiliprotein in a wealth of cyanobacteria [84] and a secondary phycobiliprotein in some red algae [85], as mentioned. Moreover, they can also be used as natural dyes in the food industry and pharmaceuticals products [86]. From direct single-molecule measurements of C-PC in EET, by monitoring the fluorescence emission from single photosynthetic antenna proteins in a free solution over a long time and within the FRET theoretical framework, it has been found that there are transitions among many different photophysical states exhibiting distinct EET pathways among the embedded pigments [87]. These numerical findings would not be accessible by bulk studies underscoring the importance of a molecular approach.

Given the present scenario of the state of the art for EET in C-PC as summarized, it would be useful to have a suitable theoretical tool to obtain both quantitative information on the EET, namely the rate constant, and a molecular-level picture of the mechanism to interpret experiments and to provide a guideline for more practical applications.

To this aim, we reformulated the original Förster theory into a set of simple formulas of directly understandable physical/chemical meaning suitable to estimate the relative contributions of the transition dipole moments of the donor and acceptor (chemical factors), their orientation factors (intermolecular structural factors), intermolecular center-to-center distances (intermolecular structural factors), spectral overlaps of the absorption and emission spectra (photophysical factors), and refractive index (material factor) thus allowing for the calculation of the EET rate constant. As a benchmark of this reformulation, we applied our formulas to the EET occurring in C-PC chromophores. The pristine structures of the C-PC chromophores, whose initial molecular structures were taken from [33], were fully optimized at the density functional theory (DFT) level, and using these resulting geometries, we computed the absorption and emission spectra along with the transition dipole moments within the time-dependent DFT (TDDFT). These results were used to apply our Förster theory reformulation to extract the EET rates and estimate quantitatively the relative contributions of the physical quantities involved in the EET process. It turns out from our results that the EET rates are determined by a balance of the specific physical, chemical, and

geometrical features of the C-PCs. These numerical examples show that our approach can potentially become a powerful tool to discriminate the relative importance of the various processes influencing the targeted system. Furthermore, this approach can provide a deeper insight into the phenomena taking place in the system. This shows that our formulas are indeed useful and provide a reasonable estimation of the relative contributions to the EET transfer rate.

2. Theoretical details

a. Quantum chemistry calculations

All the quantum chemistry calculations performed in this study have been done with the GAUSSIAN16 program package [88]. Geometry optimizations of the ground state were performed at the standard DFT framework, whereas the first excited states were obtained within the TDDFT approach [89,90]. For the exchange and correlation interactions, we used the hybrid functional B3LYP [91] and the electronic wavefunctions were represented on a 6-31G(d) basis set for both the ground and excited states during all the structural relaxations. Instead, for a refinement of the related electronic properties, namely the absorption, emission and transition dipole moments, a larger 6-311+G(d,p) basis set was used with no symmetry constraints. The protein environment around the chromphores was described by a polarizable continuum model (PCM) by setting the dielectric constant ε equal to 4.0 [92]. This approximation has been routinely adopted before and carefully benchmarked [93-96], and. we provide support to the appropriateness of this approximation in the Supporting Information. All the optimized structures represent stable local minima of the potential energy surface (PES) as confirmed by a normal modes analysis. The initial molecular structure of C-PC was obtained from the Protein Data Bank (PDB ID is 1jbo) [33]. The missing hydrogen atoms were added using GaussView 6.1 [97].

b. Calculations of EET rate constants based on the Förster theory

The original formulation of the Förster theory is based on the assumption of a weak coupling, and within this ansatz the EET rate constant, $K_{\mathrm{Förster}}$, from donor to acceptor is given by [98]:

$$K_{\mathrm{Förster}} = \frac{2\pi}{\hbar}|V_{\mathrm{F}}|^2\, J, \tag{1}$$

where J is the spectral overlap which can be calculated as

$$J = \int_a^b N_{\mathrm{A}}\, f_{\mathrm{A}}(\nu) N_{\mathrm{D}} f_{\mathrm{D}}(\nu)\mathrm{d}\nu, \tag{2}$$

and the subscripts D and A denote the donor and the acceptor, respectively. The quantities N_{A} and N_{D} are the normalization factors expressed as

$$N_{\mathrm{A}} = \frac{1}{\int_a^b f_{\mathrm{A}}(\nu)\mathrm{d}\nu}, \tag{3}$$

$$N_{\mathrm{D}} = \frac{1}{\int_a^b f_{\mathrm{D}}(\nu)\mathrm{d}\nu}, \tag{4}$$

In the above equations, ν is the frequency of light in wavenumber units (cm^{-1}) and $f_{\mathrm{A}}(\nu)$ and $f_{\mathrm{D}}(\nu)$ are the line shapes of the adsorption spectrum of the acceptor and the emission spectrum of the donor, respectively. The integration limits, a and b, are appropriately chosen such that $f_{\mathrm{A}}(\nu)$ and $f_{\mathrm{D}}(\nu)$ become almost zero in the low and high frequency limits.

The spectral overlaps, J, were obtained by integrating $f_{\mathrm{A}}(\nu)$, $f_{\mathrm{D}}(\nu)$, and $f_{\mathrm{A}}(\nu)f_{\mathrm{D}}(\nu)$ according to Eqs. (2), (3), and (4) in the range from a=500 nm to b=1200 nm (or 8.3×10^3 cm^{-1} to 2.0×10^4 cm^{-1}). The spectral shapes, $f(\nu)$, including both of $f_{\mathrm{A}}(\nu)$ and $f_{\mathrm{D}}(\nu)$, were assumed to be a superposition of the Gaussian line-shapes defined by

$$f(\nu) = f_{\max}\exp\left\{-\frac{4\ln 2}{FWHM^2}(\nu-\nu_{\max})^2\right\}, \tag{5}$$

where $f(v)$ is the oscillator strength of the absorption (emission) spectrum, f_{max} is its maximum, v_{max} is the frequency at the maximum oscillator strength, and *FWHM* is the full width at half maximum. *FWHM* was set to 4000.0 cm^{-1} in all the computational absorption and emission spectra presented in this study [82, 100].

In the dipole-dipole approximation, V_F can be written as

$$V_F = \frac{1}{4\pi\varepsilon_0}\kappa\frac{|\mu_D||\mu_A|}{n^2R^3}. \quad (6)$$

In this equation, $|\mu_D|$ and $|\mu_A|$ are the magnitudes of the transition dipole moments of D and A, respectively, which are separated by the intermolecular center-to-center distance R. In the denominator of Eq. (6), n is the refractive index of the surrounding medium [98]. The value

$$n^2 = 2 \quad (7)$$

was used [101], where n is the refractive index of the protein medium. The transition dipole moments were calculated using the Multiwfn program [102].

The orientation factor, κ, is expressed as

$$\kappa = \cos\alpha - 3\cos\beta_1\cos\beta_2, \quad (8)$$

where α is the angle between the two transition dipole moments and β_1 and β_2 are the angles between the dipoles 1 and 2 and the line joining them, respectively. The value of $|\kappa|$ ranges from 0 to 2. This situation is depicted in Figure 1.

Finally, the transfer time τ was calculated as

$$\tau = \frac{1}{K_{Förster}^{DA} + K_{Förster}^{AD}}, \quad (9)$$

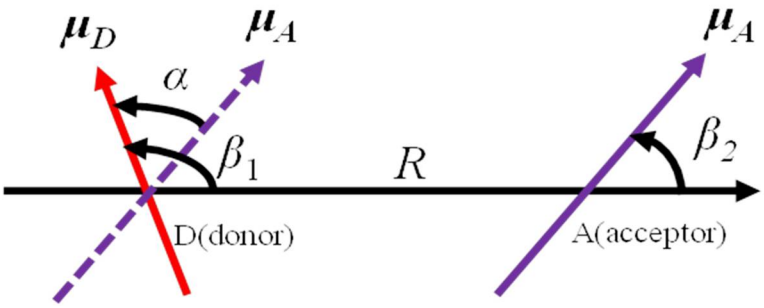

Figure 1. Schematic pictuare showing the geometric configurations of the transition dipole moments of D (donor) and A (acceptor), $\boldsymbol{\mu_D}$ and $\boldsymbol{\mu_A}$, respectively. R is the intermolecular center-to-center distance between D and A. α is the angle between the two transition dipole moments and β_1 and β_2 are the angles between dipoles 1 and 2, respectively, and the line joining them ***R***.

where $K_{Förster}^{DA}$ and $K_{Förster}^{AD}$ are the EET rate constants for the pathway from D to A and for the reverse pathway from A to D, respectively.

The aim of our study is to reformulate the above quantities, κ, μ_D and μ_A, n^2, R, J, V_F, $K_{Förster}$, and τ, expressed by the Eqs. (1), (6), and (9), into comparable quantities which would be difficult to compare because of their different units and physical meaning.

We start by defining the general idea of "contribution factor". In this respect, a physical quantity, a, which depends on some other physical variables, b_1, b_2, b_3, etc., can be written as a function of these arguments, namely

$$a = a(b_1, b_2, b_3, \ldots.). \quad (10)$$

In our specific case, we assume that a and b_i's are positive numbers. We assume that only one of the arguments, for instance b_i, is rescaled by some positive dimensionless constant B_i,

$$b_i \rightarrow B_i b_i, \quad (11)$$

, that is,

$\log_{10} b_i \rightarrow \log_{10} b_i + \log_{10} B_i$, (12)

and that as a result, the logarithm of a increases by a actor $\delta\log_{10} a$ common to all the b_i':

$\log_{10} a \rightarrow \log_{10} a + \delta\log_{10} a$. (13)

We can then define

$F_{(i)}^{a} \equiv \log_{10} B_i / \delta\log_{10} a$ (14)

as a contribution factor of a with respect to b_i. This definition of the measure of the contribution factor, $F_{(i)}^{a}$, is of practical use for at least three reasons:

(i) The logarithmic increase of a defined by Eq.(13) is proportional to and directly determined by the logarithmic increase of only one of the two variables defined by Eq.(12). Therefore, the contribution factor defined by Eq.(14) determines the amount of the contribution of the physical quantity, b_i, to a. Hence, $F_a^{(i)}$ defined by Eq. (14) provides an estimation of the effect of the presence of b_i in the physical quantity a defined by Eq. (10). This proves that $F_a^{(i)}$ is a useful and consistent definition allowing to rationalize the contribution factor of a with respect to b_i.

(ii) The contribution factor defined by Eq.(14) does not depend on any variable other than b_i.

(iii) The dimensionless logarithmic version of the quantities $\log_{10} B_i$'s, which pertain to the different physical dimensions, are the ones that can be directly compared instead of the original b_i.

To simplify our formulation and to make the different quantities less heterogeneous, we adopt the following fundamental units:

$\kappa^{(0)}$, $\mu^{(0)}$, ${n^{(0)}}^2$, $R^{(0)}$, $J^{(0)}$, $V^{(0)}$, $K^{(0)}$, and $\tau^{(0)}$ (15)

for κ, μ_{D} and μ_{A}, n^2, R, J, V_{F}, $K_{\mathrm{Förster}}$, and τ, respectively. They are defined by

$\kappa^{(0)} = 1$, (16)

$\mu^{(0)} = 1$ a.u., (17)

${n^{(0)}}^2 = 1$, (18)

$R^{(0)} = 1$ a.u., (19)

$J^{(0)} = 1$ a.u., (20)

$V^{(0)} = 1$ a.u., (21)

$K^{(0)} = 2\pi$ a.u., (22)

$\hbar = 4\pi\varepsilon_0$=1, (23)

and

$\tau^{(0)}$=1/(4 π) a.u.. (24)

Using these definitions of the fundamental units, a simple substitution of Eqs.(16)~(23) into Eqs.(1) and (6) provides the following expression:

$$\frac{K_{\mathrm{Förster}}}{K^{(0)}} = \left\{\frac{|\kappa|}{|\kappa^{(0)}|}\frac{{n^{(0)}}^2}{n^2}\frac{|\mu_{\mathrm{D}}|}{|\mu^{(0)}|}\frac{|\mu_{\mathrm{A}}|}{|\mu^{(0)}|}\left(\frac{R^{(0)}}{R}\right)^3\right\}^2\frac{J}{J^{(0)}} \quad . \tag{25}$$

Here, κ, μ_{D} and μ_{A}, n^2, R, J, V_{F}, and $K_{\mathrm{Förster}}$, are measured with respect to their own fundamental units, $\kappa^{(0)}$, $\mu^{(0)}$, ${n^{(0)}}^2$, $R^{(0)}$, $J^{(0)}$, $V^{(0)}$, and $K^{(0)}$, according to the definitions (16)~(22). Computing the logarithm of both sides of Eq.(25) leads to

$$\log_{10}\left(\frac{K_{\mathrm{Förster}}}{K^{(0)}}\right) = 2\log_{10}\frac{|\kappa|}{|\kappa^{(0)}|} + 2\log_{10}\frac{|\mu_{\mathrm{D}}|}{|\mu^{(0)}|} + 2\log_{10}\frac{|\mu_{\mathrm{A}}|}{|\mu^{(0)}|} + \log_{10}\frac{J}{J^{(0)}} - 6\log_{10}\frac{R}{R^{(0)}} - 2\log_{10}\frac{n^2}{{n^{(0)}}^2}. \tag{26}$$

Here, we have assumed that μ_{D}, μ_{A}, n^2, R, J, V_{F}, and $K_{\mathrm{Förster}}$ (or $K_{\mathrm{Förster}}^{\mathrm{DA}}$ and $K_{\mathrm{Förster}}^{\mathrm{AD}}$) are expressed in atomic units and that κ is dimensionless. Then, all of the quantities, $|\kappa|/|\kappa^{(0)}|$,

$|\mu_D|/|\mu^{(0)}|$, $|\mu_A|/|\mu^{(0)}|$, $n^2/{n^{(0)}}^2$, $R/R^{(0)}$, $J/J^{(0)}$, and $K_{\text{Förster}}/K^{(0)}$ (or $K^{\text{DA}}_{\text{Förster}}/K^{(0)}$ and $K^{\text{AD}}_{\text{Förster}}/K^{(0)}$), appearing in Eq.(26) become dimensionless. On these bases, we can compute the contribution factors of $K_{\text{Förster}}/K^{(0)}$ with respect to $|\kappa|/|\kappa^{(0)}|$, $|\mu_D|/|\mu^{(0)}|$, $|\mu_A|/|\mu^{(0)}|$, $J/J^{(0)}$, $R/R^{(0)}$, and ${n^2}/{n^{(0)}}^2$.

By multiplying $|\kappa|$, $|\mu_D|$, $|\mu_A|$, J, R, and n^2 by some arbitrary constants, C_κ, C_{μ_D}, C_{μ_A}, C_J, C_R, and C_{n^2}, and $K_{\text{Förster}}$ we can rewrite these terms as $K^{(\kappa)}_{\text{Förster}}$, $K^{(\mu_D)}_{\text{Förster}}$, $K^{(\mu_A)}_{\text{Förster}}$, $K^{(J)}_{\text{Förster}}$, $K^{(R)}_{\text{Förster}}$, and $K^{(n^2)}_{\text{Förster}}$, respectively. Thus, from the definitions (10)~(14), and (26) we get:

$$F^{K_{\text{Förster}}}_{(\kappa)} = 2\frac{\log_{10}C_\kappa}{\log_{10}D_\kappa}, \tag{27}$$

$$F^{K_{\text{Förster}}}_{(\mu_D)} = 2\frac{\log_{10}C_{\mu_D}}{\log_{10}D_{\mu_D}}, \tag{28}$$

$$F^{K_{\text{Förster}}}_{(\mu_A)} = 2\frac{\log_{10}C_{\mu_A}}{\log_{10}D_{\mu_A}}, \tag{29}$$

$$F^{K_{\text{Förster}}}_{(J)} = \frac{\log_{10}C_J}{\log_{10}D_J}, \tag{30}$$

$$F^{K_{\text{Förster}}}_{(R)} = -6\frac{\log_{10}C_R}{\log_{10}D_R}, \tag{31}$$

and

$$F^{K_{\text{Förster}}}_{(n^2)} = -2\frac{\log_{10}C_{n^2}}{\log_{10}D_{n^2}}, \tag{32}$$

where

$$D_\kappa = \frac{K^{(\kappa)}_{\text{Förster}}}{K^{(0)}}\frac{K^{(0)}}{K_{\text{Förster}}}, \tag{33}$$

$$D_{\mu_D} = \frac{K^{(\mu_D)}_{\text{Förster}}}{K^{(0)}}\frac{K^{(0)}}{K_{\text{Förster}}}, \tag{34}$$

$$D_{\mu_A} = \frac{K^{(\mu_A)}_{\text{Förster}}}{K^{(0)}}\frac{K^{(0)}}{K_{\text{Förster}}}, \tag{35}$$

$$D_J = \frac{K^{(J)}_{\text{Förster}}}{K^{(0)}}\frac{K^{(0)}}{K_{\text{Förster}}}, \tag{36}$$

$$D_R = \frac{K^{(R)}_{\text{Förster}}}{K^{(0)}}\frac{K^{(0)}}{K_{\text{Förster}}}, \tag{37}$$

and

$$D_{n^2} = \frac{K^{(n^2)}_{\text{Förster}}}{K^{(0)}}\frac{K^{(0)}}{K_{\text{Förster}}}. \tag{38}$$

Since we aim at calculating the contribution factors defined by Eq. (14), we have to compute $F^{K_{\text{Förster}}}_{(\kappa)}$, $F^{K_{\text{Förster}}}_{(\mu_D)}$, $F^{K_{\text{Förster}}}_{(\mu_A)}$, $F^{K_{\text{Förster}}}_{(J)}$, $F^{K_{\text{Förster}}}_{(R)}$, and $F^{K_{\text{Förster}}}_{(n^2)}$ only when the initial value of $K_{\text{Förster}}/K^{(0)}$ and those given by the transformations, $K^{(\kappa)}_{\text{Förster}}/K^{(0)}$, $K^{(\mu_D)}_{\text{Förster}}/K^{(0)}$, $K^{(\mu_A)}_{\text{Förster}}/K^{(0)}$, $K^{(J)}_{\text{Förster}}/K^{(0)}$, and $K^{(n^2)}_{\text{Förster}}/K^{(0)}$ are identical, as indicated by a common factor $\delta\log_{10}a$ in Eqs.(13) and (14). For instance, we can redefine:

$$\frac{K_{\text{Förster}}}{K^{(0)}} = 1, \tag{39}$$

and

$$\frac{K_{\text{Förster}}}{K^{(0)}} \equiv \frac{K^{(\kappa)}_{\text{Förster}}}{K^{(0)}} = \frac{K^{(\mu_D)}_{\text{Förster}}}{K^{(0)}} = \frac{K^{(\mu_A)}_{\text{Förster}}}{K^{(0)}} = \frac{K^{(J)}_{\text{Förster}}}{K^{(0)}} = \frac{K^{(R)}_{\text{Förster}}}{K^{(0)}} = \frac{K^{(n^2)}_{\text{Förster}}}{K^{(0)}}, \tag{40}$$

in which case, by substituting Eq.(39) into Eq.(26), one finds

$$\kappa = \kappa^{(0)}, \tag{41}$$
$$\mu_{\mathrm{D}} = \mu^{(0)}, \tag{42}$$
$$\mu_{\mathrm{A}} = \mu^{(0)}, \tag{43}$$
$$J = J^{(0)}, \tag{44}$$
$$R = R^{(0)}, \tag{45}$$
and
$$n^2 = n^{(0)^2}, \tag{46}$$
for the initial values of κ, μ_{D}, μ_{A}, J, R, and, n^2, respectively. Therefore, substituting Eqs.(41)~(46) into Eq.(11), C_κ, $C_{\mu_{\mathrm{D}}}$, $C_{\mu_{\mathrm{A}}}$, C_J, C_R, and C_{n^2} are redefined as
$$C_\kappa = \frac{|\kappa|}{|\kappa^{(0)}|}, \tag{47}$$
$$C_{\mu_{\mathrm{D}}} = \frac{|\mu_{\mathrm{D}}|}{|\mu^{(0)}|}, \tag{48}$$
$$C_{\mu_{\mathrm{A}}} = \frac{|\mu_{\mathrm{A}}|}{|\mu^{(0)}|}, \tag{49}$$
$$C_J = \frac{|J|}{|J^{(0)}|}, \tag{50}$$
$$C_R = \frac{|R|}{|R^{(0)}|}, \tag{51}$$
and
$$C_{n^2} = \frac{n^2}{n^{(0)^2}}. \tag{52}$$
Substituting Eqs. (39) and (40) and Eqs.(47)~(52) into Eq.(27)~(32), respectively, leads to
$$F_{\mathrm{or}} = \frac{2\log_{10}\frac{|\kappa|}{|\kappa^{(0)}|}}{C_{\mathrm{norm}}}, \tag{53}$$
$$F_{\mathrm{dip,D}} = \frac{2\log_{10}\frac{|\mu_{\mathrm{D}}|}{|\mu^{(0)}|}}{C_{\mathrm{norm}}}, \tag{54}$$
$$F_{\mathrm{dip,A}} = \frac{2\log_{10}\frac{|\mu_{\mathrm{A}}|}{|\mu^{(0)}|}}{C_{\mathrm{norm}}}, \tag{55}$$
$$F_{\mathrm{over}} = \frac{\log_{10}\frac{J}{J^{(0)}}}{C_{\mathrm{norm}}}, \tag{56}$$
$$F_{\mathrm{dis}} = -\frac{6\log_{10}\frac{R}{R^{(0)}}}{C_{\mathrm{norm}}}, \tag{57}$$
and
$$F_{\mathrm{ref}} = -\frac{2\log_{10}\frac{n^2}{n^{(0)^2}}}{C_{\mathrm{norm}}}, \tag{58}$$
where we have introduced the following shorthand notations,
$$F_{\mathrm{or}} \equiv F_{(\kappa)}^{K_{\mathrm{Förster}}}, \tag{59}$$
$$F_{\mathrm{dip,D}} \equiv F_{(\mu_{\mathrm{D}})}^{K_{\mathrm{Förster}}}, \tag{60}$$
$$F_{\mathrm{dip,A}} \equiv F_{(\mu_{\mathrm{A}})}^{K_{\mathrm{Förster}}}, \tag{61}$$
$$F_{\mathrm{over}} \equiv F_{(J)}^{K_{\mathrm{Förster}}}, \tag{62}$$
$$F_{\mathrm{dis}} \equiv F_{(R)}^{K_{\mathrm{Förster}}}, \tag{63}$$

$$F_{\mathrm{ref}} \equiv F_{(n^2)}^{K_{\mathrm{Förster}}}, \tag{64}$$

and

$$C_{\mathrm{norm}} \equiv \log_{10}\left(\frac{K_{\mathrm{Förster}}}{K^{(0)}}\right). \tag{65}$$

Substituting Eqs. (53)~(58) and Eq.(65) into Eq.(26), it turns out that

$$F_{\mathrm{or}} + F_{\mathrm{dip,D}} + F_{\mathrm{dip,A}} + F_{\mathrm{over}} + F_{\mathrm{dis}} + F_{\mathrm{ref}} = 1, \tag{66}$$

On the other hand, substituting Eqs.(22) and (24) into Eq.(9) leads to

$$\frac{\tau}{\tau^{(0)}} = \frac{2}{K_{\mathrm{Förster}}^{\mathrm{DA}}/K^{(0)} + K_{\mathrm{Förster}}^{\mathrm{AD}}/K^{(0)}}. \tag{67}$$

Equations (53)~(58) and Eq.(66) suggest that F_{or}, $F_{\mathrm{dip,D}}$, $F_{\mathrm{dip,A}}$, F_{over}, F_{dis}, and F_{ref}, which are the quantities dependent on the systems considered, are the magnitudes of the independent linear contributions of $|\kappa|$, $|\mu_{\mathrm{D}}|$, $|\mu_{\mathrm{A}}|$, J, R, and n^2 to $K_{\mathrm{Förster}}$, respectively.

We stress the four following points:

(i) the dimensionless logarithms of F_{or}, $F_{\mathrm{dip,D}}$, $F_{\mathrm{dip,A}}$, F_{over}, F_{dis}, and F_{ref} always sum to unity according to Eq. (66).

(ii) Here and below, the physical and chemical quantities which are the argument of the logarithm are always dimensionless as pointed out above.

(iii) Each logarithm of F_{or}, $F_{\mathrm{dip,D}}$, $F_{\mathrm{dip,A}}$, F_{over}, F_{dis}, and F_{ref} is divided by the common factor, C_{norm}. Therefore, we cannot only estimate the separate contributions of $|\kappa|$, $|\mu_{\mathrm{D}}|$, $|\mu_{\mathrm{A}}|$, J, R, and n^2 to $K_{\mathrm{Förster}}$, which are dependent on the system considered, but we can also observe that these quantities are normalized in the sense that the simple summation of the logarithms has to be equal to 1 for any system (see Eqs. (53)~(58) and Eq.(66)), and (iv) From Eq.(66), it can be remarked that if one term of the left-hand side of Eq.(66) is greater than 1/6=0.17, this term positively contributes to the EET rate. On the other hand, if it is lower than 1/6=0.17, this same term contributes negatively to the EET rate. This is a consequence of the fact that the six terms on the left-hand side of Eq.(66) always sum to unity and they have all the same relative weight.

(iv) Since we can separate the contributions of the transition dipole moments of D and A (chemical factors), their orientation factors (intermolecular structural factors), the intermolecular center-to-center distances (intermolecular structural factors), the spectral overlaps of absorption and emission (photophysical factors), and refractive index (material factor) in the form of a linear sum of the respective terms, the fundamental theory, which approximates the electronic coupling interaction V_{F} by the transition dipole approximation derived above, allows a straightforward estimation of each contribution to the EET rate. This is a practical advantage compared to the more sophisticated methods proposed in the literature [103,104]. Indeed, these methods do not explicitly calculate the single contributions of $|\kappa|$, $|\mu_{\mathrm{D}}|$, $|\mu_{\mathrm{A}}|$, R, and n^2 but directly the electronic coupling V_{F}. However, from this global coupling term, it is nearly impossible to unravel the single contributions and their relative importance in the EET process.

To calculate the contributions relative to a particular transfer pathway from D to A, e.g., from 1 to 2, the following formulas can be used:

$$F_{\mathrm{or}}^{(\mathrm{rel})} = \left.\frac{2\log_{10}\frac{|\kappa|}{|\kappa^{(0)}|}}{C_{\mathrm{norm}}}, -\frac{2\log_{10}\frac{|\kappa|}{|\kappa^{(0)}|}}{C_{\mathrm{norm}}}\right|_{1\to 2}, \tag{68}$$

$$F_{\mathrm{dip,D}}^{(\mathrm{rel})} = \left.\frac{2\log_{10}\frac{|\mu_{\mathrm{D}}|}{|\mu^{(0)}|}}{C_{\mathrm{norm}}} - \frac{2\log_{10}\frac{|\mu_{\mathrm{D}}|}{|\mu^{(0)}|}}{C_{\mathrm{norm}}}\right|_{1\to 2}, \tag{69}$$

$$F_{\mathrm{dip,A}}^{(\mathrm{rel})} = \left. \frac{2\log_{10}\frac{|\mu_A|}{|\mu^{(0)}|}}{C_{\mathrm{norm}}} - \frac{2\log_{10}\frac{|\mu_A|}{|\mu^{(0)}|}}{C_{\mathrm{norm}}} \right|_{1\to 2}, \tag{70}$$

$$F_{\mathrm{over}}^{(\mathrm{rel})} = \left. \frac{\log_{10}\frac{J}{J^{(0)}}}{C_{\mathrm{norm}}} - \frac{\log_{10}\frac{J}{J^{(0)}}}{C_{\mathrm{norm}}} \right|_{1\to 2}, \tag{71}$$

$$F_{\mathrm{dis}}^{(\mathrm{rel})} = \left. -\frac{6\log_{10}\frac{R}{R^{(0)}}}{C_{\mathrm{norm}}} + \frac{6\log_{10}\frac{R}{R^{(0)}}}{C_{\mathrm{norm}}} \right|_{1\to 2}, \tag{72}$$

and

$$F_{\mathrm{ref}}^{(\mathrm{rel})} = \left. -\frac{2\log_{10}\frac{n^2}{n^{(0)^2}}}{C_{\mathrm{norm}}} + \frac{2\log_{10}\frac{n^2}{n^{(0)^2}}}{C_{\mathrm{norm}}} \right|_{1\to 2}. \tag{73}$$

Within our proposed framework, from Eqs. (53)~(58) and Eq.(66), we always have

$$F_{\mathrm{or}}^{(\mathrm{rel})} + F_{\mathrm{dip,D}}^{(\mathrm{rel})} + F_{\mathrm{dip,A}}^{(\mathrm{rel})} + F_{\mathrm{over}}^{(\mathrm{rel})} + F_{\mathrm{dis}}^{(\mathrm{rel})} + F_{\mathrm{ref}}^{(\mathrm{rel})} = 0. \tag{74}$$

3. Results and Discussion

a. C-PCs in $(\alpha\beta)_6$ hexameric form

The PBP is mainly made up of hexameric and trimeric disks of phycobiliproteins. In Figure 2, the former case, the C-PCs in the $(\alpha\beta)_6$ hexameric form, are depicted. In this study, we only focus on the EET pathways among α^1-84, β^1-84, and β^1-155. The intermolecular center-to-center distances between α^1-84 and β^1-84, β^1-84 and β^1-155, and α^1-84 and β^1-155 connected by the purple lines are 50, 34, and 47 Å, respectively.

b. Optimized molecular structures of C-PCs

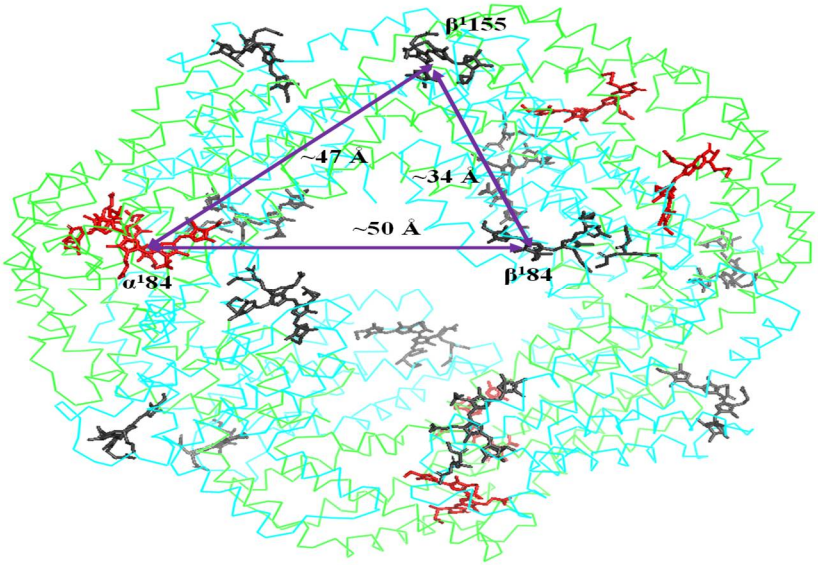

Figure 2. $(\alpha\beta)_6$ hexameric form of C-PCs. The α and β units are shown in green and light blue, respectively. The red C-PCs are those placed in the α unit whereas the gray ones are those placed in the β unit. The figure was based on the pdb data deposited in the Protein Data Bank under the accession code 1jbo [33].

To benchmark our reformulation of the Förster theory, we used the C-PC structures sketched in Figure 3, which are surrounded by the protein environment shown in Figure 4, from which our

models are derived. In Figure 3, the molecular geometry in panel (a) is identical to the model used by Ren and coworkers [82] (Figure 2 in the quoted reference), except for the crucial nearby aspartate residues (Asp-87 for α^1-84, Asp-87 for β^1-84, and Asp-39 for β^1-155) as shown in Figure 4, referred to as PCB as reported in Refs. [64, 105]. In Figure 3, the panel labeled as (b) the PCB^p model is also adopted here and has already been discussed in a former study [106]. Panel (c) of Figure 3 displays the PCB^p model with the added nearby aspartate residue [106], as shown in Figure 4. Panel (d) of Figure 3 shows a molecular structure similar to the one reported in panel (b) of Figure 3; the only difference is that the two propionic acid side-chains of the former are

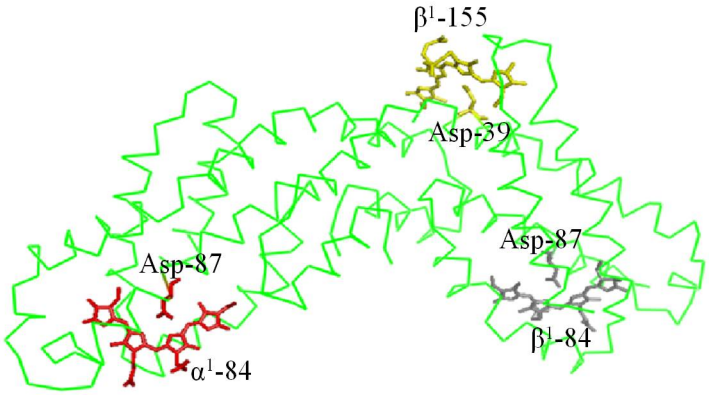

Figure 4. Crystal structure of C-PC monomer from the **t**hermophylic **c**yanobacterium *Synechococcus Elongatus* and the locations of α^1-84, β^1-84, and β^1-155, together with their neighboring aspartate residues, Asp-87, Asp-87, and Asp-39, respectively. The molecular groups, which we are interested in, α^1-84 and Asp-87, β^1-84 and Asp-87, and β^1-155 and Asp-39, are colored red, gray, and yellow, respectively. The figure was based on the pdb data deposited in the Protein Data Bank under the accession code 1jbo [3**3**].

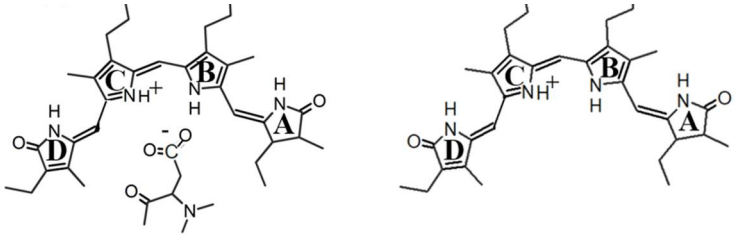

Figure 3. Computational models adopted for the structures of (a) PCB, (b) PCB^p, (c) PCB^p-asp, and (d) PCB^p-(1-).

deprotonated for the latter.

Note that the three kinds of subunits, one from the α-subunit and two from the β–subunit, are indicated as PCB1, PCB2, PCB3 for the PCB model, PCB^{p}1, PCB^{p}2, PCB^{p}3 for the PCB^p model, PCB^{p}1-asp, PCB^{p}2-asp, PCB^{p}3-asp for the PCB^p-asp model, PCB^{p}1-(1-), PCB^{p}2-(1-), PCB^{p}3-(1-) for the PCB^p-(1-) model, respectively, according to the labeling adopted in Figure 3 of Ref. [33]. Phycocyanobilins (PCBs), α-84, β-84, and β-155, described in Ref. [94] correspond to PCB1, PCB^{p}1, PCB^{p}1-asp, PCB^{p}1-(1-), PCB2, PCB^{p}2, PCB^{p}2-asp, PCB^{p}2-(1-), and PCB3, PCB^{p}3,

PCB^{p}3-asp, PCB^{p}3-(1-), respectively. The total charges of PCB (panel (a)) and PCB^{p} (panel (b)) are +1 [106], those of PCB^{p}-asp (panel (c)) are neutral [82], and those of PCB^{p}-(1-) (panel (d)) are -1. The difference between PCB and PCB^{p} consists of the fact that one β-butylene group is attached to the pyrrole ring A in the former case, while an ethyl group is attached to the pyrrole ring A in the latter case.

One of the most important features of our molecular models is that the main chain of C-PC is composed of four pyrrole rings denoted as A, B, C, and D as shown in Figure 3. The outermost two pyrrole rings, A and D, contain one oxygen atom. On the other hand, each of the other pyrrole rings, B and C, carries a propionic acid side-chain, -CH_2-CH_2-COOH, except for panel (d) of Figure 3, in which case each of the two propionic acids is deprotonated.

The optimized structures of the PCB model (PCB1, PCB2, PCB3), the PCB^{p} model (PCB^{p}1, PCB^{p}2, PCB^{p}3), and the PCB^{p}-asp model (PCB^{p}1-asp, PCB^{p}2-asp, PCB^{p}3-asp) in the ground and first excited states are shown in Figures S1, S2, and S3, respectively. Note that each PCB^{p}-(1-) model is assumed to take the molecular geometry optimized for the corresponding PCB^{p} model in this study. A feature that can be noted is that the molecular backbones composed of pyrrole rings, A, B, C and D are nearly identical in all the cases and the configurations of the two propionic acids (Figures S1 and S2) and those of the aspartate residue (Figure S3) are different for species 1, 2, and 3.

The major differences of the four models shown in panels (a), (b), (c), and (d) of Figure3 can be summarized in the following three points:, (1) the PCB has a longer conjugation length than the PCB^{p}, PCB^{p}-asp, and PCB^{p}-(1-) models, (2) the PCB^{p}-asp model includes the most important weak interaction of PCB with the respective aspartate residues, as shown in Figure 4, (3) the two propionic acids of the PCB^{p}-(1-) model are deprotonated. Therefore, comparisons among the four models can clarify the influence of the congugation length of the chromophore, the role of the weak intreaction with the aspartate residue, and the effects of the deprotonation of the propionic acids.

In particular, for the deprotonation of the propionic acids, Zienicke and coworkers experimentally investigated the photo-conversion of phytochrome Agp2 from *Agrobacterium tumefaciens*, which has a Pfr ground state and a Pr metastable state, by means of UV/visible absorption and resonance Raman spectroscopies [107]. They observed unusual spectral properties of Agp2 Pr induced by the chromophore protonation state and found that the Pfr chromophore is protonated in a range of values of the pH up to 11, while the Pr chromophore has a pK_a value of 7.6 and is therefore only partially protonated in neutral pH conditions. On the basis of these results, we can assume that some propionic acids are deprotonated while some others are protonated in the usual protein environment. On these grounds, a comparison between panels (b) and (d) of Figure 3 deserves special attention in terms of the influence of the protonation state of the propionic acids on the EET rate.

c. Absorption and emission spectra

The absorption and emission spectra of the PCB, PCB^{p}, PCB^{p}-asp, and PCB^{p}-(1-) models are shown in Figure 5. To account for the trend observed in the Q band [108,109], the values of the maximum wavelengths of the absorption and emission spectra in this same Q band have been carefully tuned for PCB1, PCB2, PCB3, PCB^{p}1, PCB^{p}2, PCB^{p}3, PCB^{p}1-asp, PCB^{p}2-asp, PCB^{p}3-asp, PCB^{p}1-(1-), PCB^{p}2-(1-), and PCB^{p}3-(1-) and these values are summarized in Table S1 together with the Stokes shifts and graphically shown in panel (f) of Figure S4.

As a first observation, we noted that the emission spectra are characerized by peaks at wavelengths slightly longer than the corresponding absorption spectra in all the cases shown in Figure 5, Table S1, and panel (f) of Figure S4. The difference in the position of the two peaks is a typical Stokes shift. From Table S1, the Stokes shifts range from 20 nm to 70 nm except for those of the PCB^{p}-(1-)_shift models. Comparing the spectral peaks of the absorption and emission spectra and the Stokes shifts among the geometries shown in Figure 3, the PCB^{p}-asp model reproduces the experimental results better than the other PCB, PCB^{p} , and PCB^{p}-(1-) ones. The wavelengths of the PCB^{p}-(1-) models are slightly shorter than or comparable to the experimental ones and those of the PCB^{p} model. Therefore, we can infer that the deprotonated and protonated propionic acids coexist under the typical experimental conditions and that the photophysical properties do not depend on the protonation state of the propionic acids.

Furthermore, we note that the wavelengths of the absorption and emission spectra undergo a shift toward the shorter values according to the order PCB, PCB^{p}, PCB^{p}-(1-), and PCB^{p}-asp, as shown in panels (a), (b), (c), and (d) of Figure 5. The fact that the PCB system has a conjugation length longer than the other three PCB^{p}, PCB^{p}-asp, and PCB^{p}-(1-) models seems to be the reason for the longer wavelengths of the absorption and emission spectra [105].

The justification in the use of the PCM instead of the real protein environment is reported in the Supporting Information.

d. Results of EET rate $K_{\text{Förster}}/K^{(0)}$ and transfer time $\tau/\tau^{(0)}$

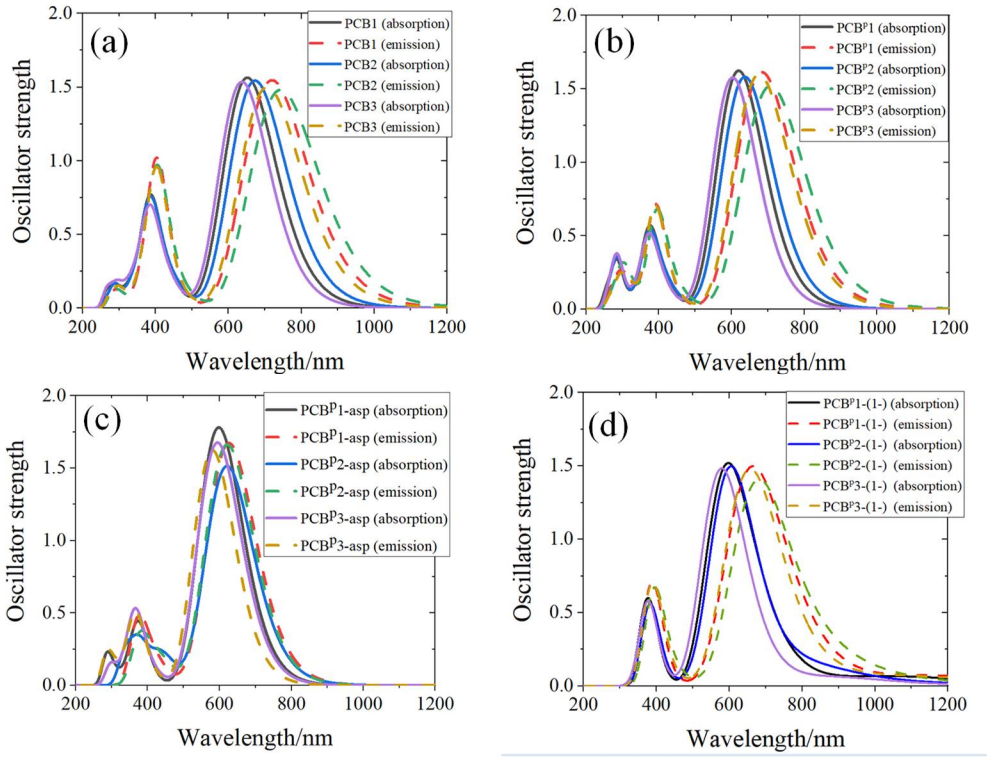

Figure 5. Calculated absorption and emission spectra of (a) PCB1, PCB2, PCB3, (b) PCB^{p}1, PCB^{p}2, PCB^{p}3, (c) PCB^{p}1-asp, PCB^{p}2-asp, PCB^{p}3-asp, and (d) PCB^{p}1-(1-), PCB^{p}2-(1-), PCB^{p}3-(1-). The calculations were done within the TDDFT framework with a B3LYP functional and the basis set 6-311+G(d,p). *FWHM* was 4000.0 cm^{-1}.

We report in Tables S2, S3, S4, and S5 all the magnitudes of the orientation factor $|\kappa|/|\kappa^{(0)}|$, the transition dipole moments of D and A, $|\mu_D|/|\mu^{(0)}|$ and $|\mu_A|/|\mu^{(0)}|$, the intermolecular center-to-center distance $R/R^{(0)}$, the square modulus of the electronic coupling $|V_F|^2/|V_F^{(0)}|^2$, the spectral overlap $J/J^{(0)}$, the EET rate constant $K_{\text{Förster}}/K^{(0)}$, inverse of $K_{\text{Förster}}/K^{(0)}$, and C_{norm} defined by Eq. (65) for the models, PCB, PCB^p, PCB^p-asp, and PCB^p-(1-) model systems, respectively. This is accompanied by a graphical presentation in panels (a), (b), (c), (d), and (e) of Figure S4 of the physical quantities, $|\kappa|/|\kappa^{(0)}|$, $|\mu_D|/|\mu^{(0)}|$ and $|\mu_A|/|\mu^{(0)}|$, $|\mu_D||\mu_A|/|\mu^{(0)}|^2$, $|V_F|^2/|V_F^{(0)}|^2$, and $J/J^{(0)}$.

From panel (d) of Figure S4, we observed that the highest value of $|V_F|^2/|V_F^{(0)}|^2$ is the one corresponding to the PCB^p-asp system, whereas it is nearly the same for the PCB and PCB^p models and it is much less for the PCB^p-(1-) model system. Moreover, $|V_F|^2/|V_F^{(0)}|^2$ is much lower for the D-A pairs, 1-3 and 3-1, than for the D-A pairs, 1-2, 2-1, 2-3, and 3-2. On the other hand, from panels (b) and (c) of Figure S4, we noted that $|\mu_D|/|\mu^{(0)}|$, $|\mu_A|/|\mu^{(0)}|$, and $|\mu_D||\mu_A|/|\mu^{(0)}|^2$ are slightly lower for the PCB^p -asp and PCB^p-(1-) model systems than those for the PCB and PCB^p systems, in which case they are significantly low for the PCB^p-(1-) model system.

From Eq. (6), $|V_F|^2$ is determined by $|\kappa|$, $|\mu_D|$, $|\mu_A|$, and R. By considering that the numerical values of $R/R^{(0)}$ are 96.0, 68.0, and 91.0 for the D-A pairs, 1-2 and 2-1, 2-3 and 3-2, and 1-3 and 3-1, respectively (see Tables S2, S3, S4, and S5), it becomes evident that the lowest values of $|V_F|^2$ for the D-A pairs, 1-3 and 3-1, are due to the higher value of $R/R^{(0)}$, and simultaneously, to the lower values of $|\kappa|/|\kappa^{(0)}|$ and $|\mu_D||\mu_A|/|\mu^{(0)}|^2$ for the pairs, 1-3 and 3-1 (see panels (a) and (c) of Figure S4).

In addition, we noted that the values of $|V_F|^2/|V_F^{(0)}|^2$ for the D-A pairs 1-2 and 2-1 are similar for the PCB, PCB^p, and PCB^p-asp models, whereas those for the PCB^p-(1-) model are lower than the other cases. Furthermore, $|V_F|^2/|V_F^{(0)}|^2$ for the D-A pairs 2-3 and 3-2 are the highest for the PCB^p-asp system and lowest for the PCB^p-(1-) system. Those of the PCB and PCB^p models are comparable and lie between those of the PCB^p-asp and PCB^p-(1-) systems as shown in panel (d) of Figure S4. These facts result from the lowest magnitudes of the transition dipole moments for the PCB^p-(1-) system, as shown in panels (b) and (c) of Figure S4.

From panel (e) of Figure S4 and Tables S2, S3, S4, and S5, we noted that the magnitudes of $J/J^{(0)}$ are roughly comparable for all the systems, PCB, PCB^p, PCB^p-asp, and PCB^p-(1-). This simply reflects the fact that the linewidth of 4000.0 cm^{-1} adopted in Figure 5 is so broad that the values of the $J/J^{(0)}$'s computed by Eq. (2) are nearly identical for all the considered molecular models and calculation levels. If we take this fact into account, $K_{\text{Förster}}/K^{(0)}$ might display a trend similar to $|V_F|^2/|V_F^{(0)}|^2$ because $K_{\text{Förster}}$ is proportional to the product of $|V_F|^2$ and J (see Eq. (1)).

This is indeed the case. The magnitudes of $K_{\text{Förster}}/K^{(0)}$ shown in panel (a) of Figure 6 show a trend analogous to the case of $|V_F|^2/|V_F^{(0)}|^2$ reported in panel (d) of Figure S4.

The transfer times for the four systems, PCB, PCB^p, PCB^p-asp, and PCB^p-(1-), calculated according to Eq. (67) are reported in panel (b) of Figure 6. The equation indicates that lower values of $K_{\text{Förster}}/K^{(0)}$ lead to higher values of the transfer times, $\tau/\tau^{(0)}$. Indeed, a simple comparison of panels (a) and (b) of Figure 6 shows that this is the overall picture. The EET rates of the PCB^p-(1-) system are the lowest among the four models. The transfer times for PCB^p-asp are shorter than those for PCB, PCB^p, and PCB^p-(1-), as shown in panel (b) of Figure 6. Furthermore, the transfer

times for the D-A pair 1-3 are much longer than those for the other D-A pairs, 1-2 and 2-3. It should be stressed that the PCB^{p}-asp model system is able to reproduce the experimental transfer time better than the PCB, PCB^{p}, and PCB^{p}-(1-) models, as shown in panel (b) of Figure 6. Given this scenario, this underlines the importance of the intermolecular interaction between PCB and the aspartate residue for a good reproduction of the experimental EET rates and transfer times, whereas the deprotonation of the propionic acids decreases the EET rates and leads to a much worse estimation of the transfer time for the D-A pair 1-3.

e. Determination of the contributions of orientation $|\boldsymbol{\kappa}|/|\boldsymbol{\kappa}^{(0)}|$, transition dipole moments, $|\mu_D|/|\mu^{(0)}|$ and $|\mu_A|/|\mu^{(0)}|$, spectral overlap $\boldsymbol{J}/\boldsymbol{J}^{(0)}$, intermolecular center-to-center distance $\boldsymbol{R}/\boldsymbol{R}^{(0)}$, and refractive index $\boldsymbol{n}^2/\boldsymbol{n}^{(0)2}$ to the EET rate constant $\boldsymbol{K}_{\text{Förster}}/\boldsymbol{K}^{(0)}$ according to the Förster theory in the C-phycocyanin chromophores

The various contributions indicated as F_{or}, $F_{\text{dip,D}}$, $F_{\text{dip,A}}$, F_{over}, F_{dis}, and F_{ref} (see Eqs. (53)~(58))

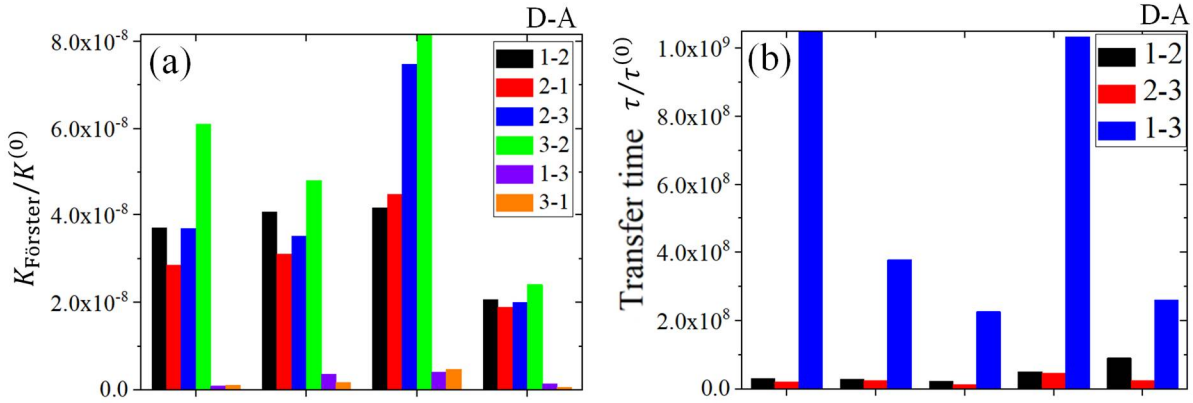

Figure 6. Calculated EET rate constants (panel (a)) and transfer times (panel (b)) of PCB, PCB^{p}, PCB^{p}-asp, and PCB^{p}-(1-) model systems adopted in this study. The calculations were carried at the TDDFT level with a hybrid functional B3LYP for the exchnage-correlation and a 6-311+G(d,p) basis set. Experimental results (Exp.) were taken from Ref. [80].

are shown in panel (a) of Figure 7 for the EET pathways, 1→2, 2→1, 2→3, 3→2, 1→3, and 3→1, for the PCB^{p}-asp system and those are shown in panels (a) of Figures S5, S6, and S7 for the PCB, PCB^{p}, and PCB^{p}-(1-) models, respectively. On the other hand, panels (b) of Figures 7, S5, S6, and S7 show $F_{\text{or}}^{(\text{rel})}$, $F_{\text{dip,D}}^{(\text{rel})}$, $F_{\text{dip,A}}^{(\text{rel})}$, $F_{\text{over}}^{(\text{rel})}$,$F_{\text{dis}}^{(\text{rel})}$, and $F_{\text{ref}}^{(\text{rel})}$ calculated according to Eqs. (68)~(73) for the EET pathways, 2→1, 2→3, 3→2, 1→3, and 3→1, in the case of the PCB^{p}-asp, PCB, PCB^{p}, and PCB^{p}-(1-) models, respectively. From panels (a) of Figures 7, S5, S6, and S7, we can note that the contribution from F_{dis} is the dominating feature in comparison to F_{or}, $F_{\text{dip,D}}$, $F_{\text{dip,A}}$, F_{over}, and F_{ref} for all the EET pathways because F_{dis} has the highest positive value. This is not entirely unexpected because the intermolecular center-to-center distance $R/R^{(0)}$ is usually the dominant factor for the EET rate constant, $K_{\text{Förster}}/K^{(0)}$.

In addition, we noticed that $F_{\text{dip,D}}$ and $F_{\text{dip,A}}$ remain nearly constant while changing the EET pathways. This implies that the variations in the order of the magnitude of $|\mu_D|/|\mu^{(0)}|$ and

$|\mu_A|/|\mu^{(0)}|$ for the different EET pathways are almost negligible as shown in panels (b), and (c) of Figure S4. The contributions of F_{ref} are nearly identical in all the cases.

An important point to make in panel (a) of Figure 7 is that F_{or} is rather low, yet its sign changes from negative to positive as the EET pathway changes as 1→2, 2→1, 2→3, 3→2, 1→3, and 3→1. This tendency is reflected in the increasing trend of the relative magnitude of $F_{\mathrm{or}}^{(\mathrm{rel})}$ as the EET pathway proceeds along 2→1, 2→3, 3→2, 1→3, and 3→1, as shown in panel (b) of Figure 7, despite the smaller simultaneous increase in $F_{\mathrm{dip,D}}^{(\mathrm{rel})}$, $F_{\mathrm{dip,A}}^{(\mathrm{rel})}$, and $F_{\mathrm{over}}^{(\mathrm{rel})}$. This can be rationalized by the direct consideration of C_{norm}. When this term is negative as in the case of Figure 7 (see Table S4) , we get $|\kappa|/|\kappa^{(0)}| < 1$ for the EET pathways, 2→3, 3→2, 1→3, and 3→1; conversely, when $|\kappa|/|\kappa^{(0)}| > 1$ as in the case of pathways, 1→2, and 2→1, as shown in panel (a) of Figure S4 for PCB$^{\mathrm{p}}$-asp, F_{or} is negative for the EET pathways, 1→2, and 2→1 and it is positive for the EET pathways, 2→3, 3→2, 1→3, and 3→1.

The reason why F_{or} increases as the EET pathways evolves along 2→3 and 3→2 to 1→3 and 3→1 can be identified in the fact that $|\kappa|/|\kappa^{(0)}|$, which is lower than 1 for the EET pathways 2→3, 3→2, 1→3, and 3→1, decreases as the EET pathways change from 2→3 and 3→2 to 1→3 and 3→1, as shown in panel (a) of Figure S4.

In addition, the reason for the change of sign in the F_{or} from the negative to the positive values as the EET pathways proceeds from 1→2 and 2→1 to 2→3 and 3→2 is that $|\kappa|/|\kappa^{(0)}|$ is lower than 1 for the EET pathways 2→3 and 3→2, whereas it becomes greater than 1 for the EET pathways 1→2 and 2→1, and C_{norm} is negative for the case described in Figure 7, in agreement with Eqs.(53) and (65). All these results indicate that F_{or} increases, assuming that the values of which are initially negative, then become positive along the EET pathways going from 1→2 and 2→1 to 2→3 and 3→2.

From panels (a) and (b) of Figure 7, we note that F_{or} increases as F_{dis} decreases, and $F_{\mathrm{or}}^{(\mathrm{rel})}$ increases as $F_{\mathrm{dis}}^{(\mathrm{rel})}$ decreases as the EET pathway evolves along the steps 1→2, 2→1, 2→3, 3→2, 1→3, and 3→1. This also has a direct explanation; the facts that C_{norm} is negative in the case shown in Figure 7 (see Table S4) and that the the magnitude of $R/R^{(0)}$ increases as the D-A combination changes from 2-3 to 1-3 to 1-2 lead to an increase of F_{dis} from 2-3 or 1-3 to 1-2 (see Eq. (65)). At the same time, $F_{\mathrm{dip,D}}$, $F_{\mathrm{dip,A}}$, and F_{over} always remain almost constant. The consequence is that the sum of the two contributions, F_{or} and F_{dis}, is nearly constant (see Eq.(65)), and, as a result, a simultaneous increase in F_{or} or $F_{\mathrm{or}}^{(\mathrm{rel})}$ and decrease in F_{dis} or $F_{\mathrm{dis}}^{(\mathrm{rel})}$ occur.

The four models shown in Figure 3 are some models of C-PCs currently used for calculations of various properties of C-PCs. As mentioned, the fact that the PCB model system has a conjugation length longer than the PCB$^{\mathrm{p}}$ seems to be the reason for the longer wavelengths of the absorption and emission spectra with respect to the former [105]. This leads to quite different relative contributions of the spectral overlap $J/J^{(0)}$ to $K_{\mathrm{Förster}}/K^{(0)}$ among the D-A pathways, 2→1, 2→3, 3→2, 1→3, and 3→1, for the PCB and PCB$^{\mathrm{p}}$ systems, as shown in panels (b) of Figure S5 and

Figure S6, respectively. In other words, the difference in $K_{\mathrm{Förster}}/K^{(0)}$ for the D-A pathways in the PCB and PCB$^{\mathrm{p}}$ systems mainly arises from the different relative contributions from the spectral overlap, $J/J^{(0)}$, which in turn originates from the different conjugation lengths. In addition, such a difference leads to a significantly different transfer time for the D-A combination of 1-3 shown by the blue bars in panel (b) of Figure 6 for the PCB and PCB$^{\mathrm{p}}$ systems.

Based on these considerations, the comparison between the PCB (panel (a) of Figure 3) and PCB$^{\mathrm{p}}$ (panel (b) of Figure3) systems provides a clear example in which the difference in the spectral overlap $J/J^{(0)}$ originating from the different conjugation length plays a key role in discriminating the relative contributions to the EET rate, $K_{\mathrm{Förster}}/K^{(0)}$, for the different D-A pathways.

On the other hand, panels (b) and (c) of Figure 5 show that the PCB$^{\mathrm{p}}$ and PCB$^{\mathrm{p}}$-asp systems have a very different photoresponse; specifically, the absorption and emission wavelengths. This is due to the presence/absence of the weak interaction between the chromophore and aspartate residue, which is similar to the comparison between the PCB and PCB$^{\mathrm{p}}$ systems although the chemical origins are different. Unlike the comparison between these PCB and PCB$^{\mathrm{p}}$ systems, the difference in the relative contributions of the orientation factors to $K_{\mathrm{Förster}}/K^{(0)}$ among the D-A pathways, 2→1, 2→3, 3→2, 1→3, and 3→1, is more important for the PCB system than that from the spectral overlap in the PCB$^{\mathrm{p}}$ and PCB$^{\mathrm{p}}$-asp systems, as shown in panels (b) of Figure S6 and Figure 7. At the same time, the relative contribution from the center-to-center distance for both the PCB$^{\mathrm{p}}$ and PCB$^{\mathrm{p}}$-asp systems proportionately decreases. This compensation leads to the transfer times for the D-A combinations, 1-2, 2-3, and 1-3, which are similar and reproduce the experimental values better for the PCB$^{\mathrm{p}}$ and PCB$^{\mathrm{p}}$-asp systems. Conversely, those are rather different between the PCB and PCB$^{\mathrm{p}}$ (1-) systems and the PCB$^{\mathrm{p}}$ and PCB$^{\mathrm{p}}$-asp systems.

Based on these considerations, the comparison among the systems PCB (panel (a) of Figure 3), PCB$^{\mathrm{p}}$ (panel (b) of Figure 3), and PCB$^{\mathrm{p}}$-asp (panel (c) of Figure 3) provides a typical example where the difference in the transfer times originates from the difference in the orientation factor. Moreover, the comparison between PCB$^{\mathrm{p}}$ (panel (b) of Figure 3) and PCB$^{\mathrm{p}}$-asp (panel (c) of Figure 3) shows that there is a compensation among the factors (orientation factor and center-to-center distance factor in this case), which leads to the similar transfer times for the D-A combinations, 1-2, 2-3, and 1-3.

Finally, the comparison between PCB^{p} (panel (b) of Figure 3) and PCB^{p}-(1-) (panel (d) of Figure 3) shows that the deprotonation of the two adjacent propionic acids leads to a decrease of the EET rates, which in turn originates from the small transition dipole moments of the deprotonated PCB systems.

In summary, by using Eqs. (53)~(58) and Eqs.(65)~(74) derived in this study, the following key points have been concluded for the EET in the C-PC chromophores:

(i) The EET rate constant $K_{\text{Förster}}/K^{(0)}$ is dominated by the intermolecular center-to-center

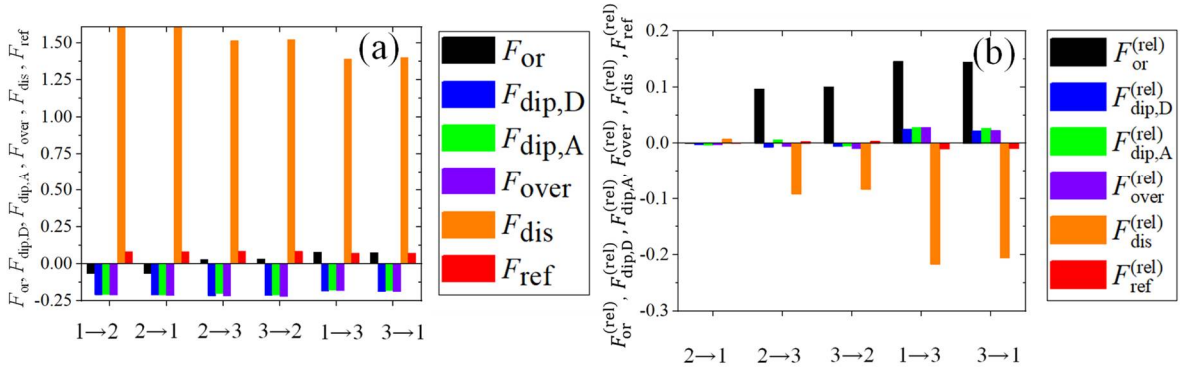

Figure 7. Panel (a): F_{or}, $F_{dip,D}$, $F_{dip,A}$, F_{over}, F_{dis}, and F_{ref} as obtained from Eqs. (14)~(18) for the EET pathways, 1→2, 2→1, 2→3, 3→2, 1→3, and 3→1, for the PCB^{p}-asp system. Panel (b): $F^{(rel)}_{or}$, $F^{(rel)}_{dip,D}$, $F^{(rel)}_{dip,A}$, $F^{(rel)}_{over}$, $F^{(rel)}_{dis}$, and $F^{(rel)}_{ref}$ calculated according to Eqs. (68)~(73) for the EET pathways, 2→1, 2→3, 3→2, 1→3, and 3→1, for the PCB^{p}-asp.

distance $R/R^{(0)}$.

(ii) The quantities, $|\mu_D|/|\mu^{(0)}|$, $|\mu_A|/|\mu^{(0)}|$, and $J/J^{(0)}$. remain almost constant for any of the EET pathways. This implies that their coontributions to the EET rate constant remain unchanged for any of the EET pathways.

(iii) From (i), (ii), and according to Eq. (65), the change in $R/R^{(0)}$ as shown in panel (a) of Figure 7 is compensated by $|\kappa|/|\kappa^{(0)}|$. Thus, F_{or} increases as F_{dis} decreases, and, analogously, $F^{(rel)}_{or}$ increases as $F^{(rel)}_{dis}$ decreases.

(iv) The relative contributions of the orientation factors $|\kappa|/|\kappa^{(0)}|$ are also non-negligible as reported in panel (b) of Figure 7. This implies that the balance between $|\kappa|/|\kappa^{(0)}|$ and $R/R^{(0)}$ determines the EET rate constant $K_{\text{Förster}}/K^{(0)}$ in the case of the PCB^{p}-asp system.

(v) The influence of the difference in the conjugation length was evidenced by comparing the PCB and PCB^{p} systems. The longer conjugation length leads to a greater relative contribution from the spectral overlap than from the other factors, which finally results in a longer transfer time.

(vi) The influence of the difference in the orientation factor of the transition dipole moment was rationalized by comparing the PCB system and PCB^{p} and PCB^{p}-asp systems. In this case, such a difference leads to different transfer times.

(vii) The compensation of the factors was found by the comparison between the PCB^{p} and PCB^{p}-asp systems. The orientation factor and that of the center-to-center distance compensate each other, which leads to similar transfer times for the D-A combinations, 1-2, 2-3, and 1-3.

(viii) By comparing the PCB^p-asp and PCB^p-(1-) systems, it turns out that the deprotonation of the two adjacent propionic acids leads to a decrease in the EET rates, and this originates from the lower transition dipole moments of the deprotonated PCB^p-(1-) system.

In conclusion, we have shown that a logarithmic reformulation (Eq. (1)) of the original Förster theory allows splitting of all the single contributions, expressed by Eqs. (66) and (74), and this formulation, in turn, leads to a simple linear addition of the separated terms. Each term has an intuitive physical and chemical interpretation and allows to rationalize the various contributions affecting the EET rate constant, which is not necessarily evident if one only relies on the product form of Eq.(1).

Finally, an extension of our method to the case where both the Förster and Dexter theories play a role in the EET process is described in the Supporting Information.

4. Conclusions

In this study, we have shown that a simple logarithmic reformulation of the theoretical approach originally proposed by Förster leads to a set of simple and convenient formulas useful to separate the four different contributions, namely (i) transition dipole moments of the donor and acceptor (chemical factors), (ii) their orientation factors (structural factors), (iii) intermolecular center-to-center distances (structural factors), (iv) spectral overlaps of the absorption and emission spectra (photophysical factors), and (v) refractive index (material factor), all of them involved in the determination of the excitation energy transfer (EET) rate constant. To demonstrate the applicability of this reformulation, we focused on the EET pairs in the C-phycocyanin (C-PC) chromophores. Quantum chemical calculations based on DFT were done to obtain optimized molecular structures. The absorption and emission spectra, and transition dipole moments were evaluated by a TDDFT approach. The obtained results show that our formulas are indeed versatile and provide a deeper insight into the physical and chemical origins contributing to the EET rate.

Our method is prone to become useful for the design of high-efficiency solar cells, artificial photosynthesis systems, etc., because it can quantify the relative magnitudes of the contributions involved in the EET rates and their constructive or destructive effects. This, in turn, allows to unravel which parameters require special attention and optimization.

As an added value, we remark that the method proposed here may become particularly useful if the number of parameters included in the formula of the EET rate increases, since it is not necessarily clear what kind of balance of the parameters determines the EET rate if one makes use of the original formula.

ASSOCIATED CONTENT

Supporting Information.

The following files are available free of charge.

Front and side views of the optimized geometries for the ground state of PCB1, the first excited state of PCB1, the ground state of PCB2, the first excited state of PCB2, the ground state of PCB3, and the first excited state of PCB3 (Figure S1).

Front and side views of the optimized geometries for the ground state of PCB^p1, the first excited state of PCB^p1, the ground state of PCB^p2, the first excited state of PCB^p2, the ground state of PCB^p3, and the first excited state of PCB^p3 (Figure S2).

Front and side views of the optimized geometries for the ground state of PCB^{p}1-asp, the first excited state of PCB^{p}1-asp, the ground state of PCB^{p}2-asp, the first excited state of PCB^{p}2-asp, the ground state of PCB^{p}3-asp, and the first excited state of PCB^{p}3-asp (Figure S3).

Physical quantities related to the expression of the EET rate as formulated in Eq. (1) for PCB, PCB^{p}, PCB^{p} -asp, and PCB^{p}-(1-): $|\kappa|/|\kappa^{(0)}|$, $|\mu_D|/|\mu^{(0)}|$, $|\mu_A|/|\mu^{(0)}|$, $|\mu_D||\mu_A|/|\mu^{(0)}|^2$, $|V_F|^2/|V_F^{(0)}|^2$, $J/J^{(0)}$, and peak wavelengths of absorption and emission spectra in Q band shown Figure 5 and Table S1 (Figure S4).

Factors, F_{or}, $F_{dip,D}$, $F_{dip,A}$, F_{over}, F_{dis}, and F_{ref} as obtained from Eqs. (53)~(58) for the EET pathways, 1→2, 2→1, 2→3, 3→2, 1→3, and 3→1, and factors, $F_{or}^{(rel)}$, $F_{dip,D}^{(rel)}$, $F_{dip,A}^{(rel)}$, $F_{over}^{(rel)}$, $F_{dis}^{(rel)}$, and $F_{ref}^{(rel)}$ calculated according to Eqs. (68)~(73) for the EET pathways, 2→1, 2→3, 3→2, 1→3, and 3→1, for the PCB system (Figure S5).

Factors, F_{or}, $F_{dip,D}$, $F_{dip,A}$, F_{over}, F_{dis}, and F_{ref} as obtained from Eqs. (53)~(58) for the EET pathways, 1→2, 2→1, 2→3, 3→2, 1→3, and 3→1, and factors, $F_{or}^{(rel)}$, $F_{dip,D}^{(rel)}$, $F_{dip,A}^{(rel)}$, $F_{over}^{(rel)}$, $F_{dis}^{(rel)}$, and $F_{ref}^{(rel)}$ calculated according to Eqs. (68)~(73) for the EET pathways, 2→1, 2→3, 3→2, 1→3, and 3→1, for the PCB^{p} model (Figure S6).

Factors, F_{or}, $F_{dip,D}$, $F_{dip,A}$, F_{over}, F_{dis}, and F_{ref} as obtained from Eqs. (53)~(58) for the EET pathways, 1→2, 2→1, 2→3, 3→2, 1→3, and 3→1, and factors, $F_{or}^{(rel)}$, $F_{dip,D}^{(rel)}$, $F_{dip,A}^{(rel)}$, $F_{over}^{(rel)}$, $F_{dis}^{(rel)}$, and $F_{ref}^{(rel)}$ calculated according to Eqs. (68)~(73) for the EET pathways, 2→1, 2→3, 3→2, 1→3, and 3→1, for the PCB^{p}-(1-) model (Figure S7).

Calculated absorption and emission spectra of PCB^{p}1-(1-)_shift, PCB^{p}2-(1-)_shift, and PCB^{p}3-(1-)_shift (Figure S8).

Factors, F_{or}, $F_{dip,D}$, $F_{dip,A}$, F_{over}, F_{dis}, and F_{ref} as obtained from Eqs. (53)~(58) for the EET pathways, 1→2, 2→1, 2→3, 3→2, 1→3, and 3→1, and factors, $F_{or}^{(rel)}$, $F_{dip,D}^{(rel)}$, $F_{dip,A}^{(rel)}$, $F_{over}^{(rel)}$, $F_{dis}^{(rel)}$, and $F_{ref}^{(rel)}$ calculated according to Eqs. (68)~(73) for the EET pathways, 2→1, 2→3, 3→2, 1→3, and 3→1, for the PCB^{p}-(1-)_shift system (Figure S9).

EET rates, $K_{Förster}/K^{(0)}$, $K_{Dexter}/K^{(0)}$, and $K_{EET}/K^{(0)}$, versus the intermolecular distance $R/R^{(0)}$, in P3HT/PCBM blend (Figure S10).

Relative importance of the physical quantities related to EET rate, $K_{EET}/K^{(0)}$, versus the intermolecular distance $R/R^{(0)}$ in P3HT/PCBM blend (Figure S11).

Maximum wavelengths of absorption and emission spectra, and Stokes shifts in Q band for PCB1, PCB2, PCB3 PCB^{p}1, PCB^{p}2, PCB^{p}3, PCB^{p}1-asp, PCB^{p}2-asp, PCB^{p}3-asp, PCB^{p}1-(1-), PCB^{p}2-(1-), and PCB^{p}3-(1-) shown in Figure 5, and PCB^{p}1-(1-)_shift, PCB^{p}2-(1-)_shift, and PCB^{p}3-(1-)_shift. (Table S1).

Magnitudes of orientation factor $|\kappa|/|\kappa^{(0)}|$, transition dipole moments of D and A $|\mu_D|/|\mu^{(0)}|$ and $|\mu_A|/|\mu^{(0)}|$, intermolecular center-to-center distance $R/R^{(0)}$, square of the the electronic coupling $|V_F|^2/|V_F^{(0)}|^2$, spectral overlap $J/J^{(0)}$, EET rate constant $K_{Förster}/K^{(0)}$, inverse of $K_{Förster}/K^{(0)}$, and C_{norm} for the PCB systems, PCB1, PCB2, and PCB3 (Table S2).

Magnitudes of orientation factor $|\kappa|/|\kappa^{(0)}|$, transition dipole moments of D and A $|\mu_D|/|\mu^{(0)}|$ and $|\mu_A|/|\mu^{(0)}|$, intermolecular center-to-center distance $R/R^{(0)}$, square of the the electronic coupling $|V_F|^2/|V_F^{(0)}|^2$, spectral overlap $J/J^{(0)}$, EET rate constant $K_{Förster}/K^{(0)}$, inverse of $K_{Förster}/K^{(0)}$, and C_{norm} for the PCB^{p} systems, PCB^{p}1, PCB^{p}2, and PCB^{p}3 (Table S3).

Magnitudes of orientation factor $|\kappa|/|\kappa^{(0)}|$, transition dipole moments of D and A $|\mu_D|/|\mu^{(0)}|$ and $|\mu_A|/|\mu^{(0)}|$, intermolecular center-to-center distance $R/R^{(0)}$, square of the the electronic coupling $|V_F|^2/|V_F^{(0)}|^2$, spectral overlap $J/J^{(0)}$, EET rate constant $K_{\text{Förster}}/K^{(0)}$, inverse of $K_{\text{Förster}}/K^{(0)}$, and C_{norm} for the PCB$^{\text{p}}$-asp systems, PCB$^{\text{p}}$1-asp, PCB$^{\text{p}}$2-asp, and PCB$^{\text{p}}$3-asp. (Table S4).
Magnitudes of orientation factor $|\kappa|/|\kappa^{(0)}|$, transition dipole moments of D and A $|\mu_D|/|\mu^{(0)}|$ and $|\mu_A|/|\mu^{(0)}|$, intermolecular center-to-center distance $R/R^{(0)}$, square of the the electronic coupling $|V_F|^2/|V_F^{(0)}|^2$, spectral overlap $J/J^{(0)}$, EET rate constant $K_{\text{Förster}}/K^{(0)}$, inverse of $K_{\text{Förster}}/K^{(0)}$, and C_{norm} for the PCB$^{\text{p}}$-(1-) systems, PCB$^{\text{p}}$1-(1-), PCB$^{\text{p}}$2-(1-), and PCB$^{\text{p}}$3-(1-). (Table S5).
Magnitudes of orientation factor $|\kappa|/|\kappa^{(0)}|$, transition dipole moments of D and A $|\mu_D|/|\mu^{(0)}|$ and $|\mu_A|/|\mu^{(0)}|$, intermolecular center-to-center distance $R/R^{(0)}$, square of the the electronic coupling $|V_F|^2/|V_F^{(0)}|^2$, spectral overlap $J/J^{(0)}$, EET rate constant $K_{\text{Förster}}/K^{(0)}$, inverse of $K_{\text{Förster}}/K^{(0)}$, and C_{norm} for the PCB$^{\text{p}}$-(1-)_shift systems, PCB$^{\text{p}}$1-(1-)_shift, PCB$^{\text{p}}$2-(1-)_shift, and PCB$^{\text{p}}$3-(1-)_shift. (Table S6).

AUTHOR INFORMATION

Author Contributions

The manuscript was written through contributions of all authors. K.M., derivations of equations, quantum chemistry calculations, and writing original draft. M.S., conceptualization, investigation, editing and funding acquisition. Y.U, M.B, and Y.S., investigation and editing.

Funding Sources

This research was supported by Japan Science and Technology Agency (JST), PRESTO Grant Number JPMJPR19G6, Japan, and Japan Society for the Promotion of Science (JSPS) Grants-in-Aid for Scientific Research (KAKENHI) Grant Numbers JP17H04866, JP20H05088 and JP20H05453. M.B. thanks the HPC Mesocentera at the University of Strasbourg funded by the Equipex Equip@Meso project (Programme Investissements d'Avenir) and the CPER Alsacalcul/Big Data, and the Grand Equipement National de Calcul Intensif (GENCI) under allocation DARI-A0100906092.

ACKNOWLEDHGEMENTS

Numerical calculations were carried out under support from the “Multidisciplinary Cooperative Research Program” at the Center for Computational Sciences (CCS) in University of Tsukuba.

REFERENCES

1 Chaiklahan, R.; Chirasuwan, N.; Loha, V.; Tia, A.; Bunnag, B. Separation and purification of phycocyanin from Spirulina sp. using a membrane process. *Bioresour. Technol*. **2011**, *102*, 7159-7164.
2 Scheer, H.; Zhao, K.H. Biliprotein maturation: the chromophore attachment. *Mol. Microbiol*. **2008**, *68*, 1263-1276.
3 Glazer, A.N. Phycobiliproteins—a family of valuable, widely used fluorophores. *J. Appl. Phycol*. **1994**, *6*, 105–112.
4 Sun, L.; Wang, S.; Chen, L.; Gong, X. Promising fluorescent probes from phycobiliproteins. *IEEE. J. Sel. Top. Quantum. Electron*. **2003**, *9*, 177–188.

5 Glazer, A.N. Directional energy transfer in a photosynthetic antenna. *J. Biol. Chem.* **1989**, *264*, 1–4.
6 Petrášek, Z.; Schmitt, F.-J.; Theiss, C.; Huyer, J.; Chen, M.; Larkum, A.; Eichler, H.J.; Kemnitz, K.; Eckert, H.-J. Excitation energy transfer from phycobiliprotein to chlorophyll *d* in intact cells of *Acaryochloris marina* studied by time- and wavelength-resolved fluorescence spectroscopy. *Photochem. Photobiol. Sci.* **2005**, *4*, 1016-1022.
7 Glazer, A.N.; Apell. G.S.; Hixson, C.S.; Bryant, D.A.; Brown, D.M. Biliproteins of and Rhodophyta: Homologous family of photosynthetic accessory pigment. *Proc. Nat. Acad. Sci. USA*. **1976**, *73*, 428-431.
8 Gantt, E. Phycobilisomes. *Annu. Rev. Plant. Physiol.* **1981**, *32*, 327–347.
9 Bryant, D. A. Cell Culture and Somatic Cell Genetics of Plants, Vol. 7B (L. Bogorad and I. K. Vasil, editors). Academic Press, New York, London. **1991**, 257–330. Chang, W., T. Jiang, Z.
10 Glazer, A.N.; Hixson, C.S. Characterization of R-phycocyanin. Chromophore content of R-phycocyanin and C-phycoerythrin, *J. Biol. Chem.* **1975**, *250*, 5487–5495.
11 Oi, V.T.; Glazer, A.N.; Stryer, L. Fluorescent phycobiliprotein conjugates for analyses of cells and molecules. *J. Cell. Biol.* **1982**, *93*, 981–986.
12 Glazer, A.N.; Stryer, L. Fluorescent tandem phycobiliprotein conjugates. emission wavelength shifting by energy transfer. *Biophys. J.* **1983**, *43*:383–386.
13 Loos, D.; Cotlet, M.; Schryver, F.D.; Habuchi, S.; Hofkens, J. Single-molecule spectroscopy selectively probes donor and acceptor chromophores in the phycobiliprotein allophycocyanin. *Biophys. J.* **2004**, *87*, 2598–2608.
14 Wolf, E.; Schübler, A. Phycobiliprotein fluorescence of *Nostoc punctiforme* changes during the life cycle and chromatic adaptation: characterization by spectral confocal laser scanning microscopy and spectral unmixing. *Plant Cell Environ.* **2005**, *28*, 480–491.
15 Isailovic, D.; Sultana, I,; Phillips, G.J.; Yeung, E.S. Formation of fluorescent proteins by the attachment of phycoerythrobilin to R-phycoerythrin alpha and beta apo-subunits. *Anal. Biochem.* **2006**, *358*, 38–50.
16 Chen, Z.; Kaplan, D.L.; Yang, K.; Kumar, J.; Marx, K.A.; Tripathy, S.K. Two-photon-induced fluorescence from the phycoerythrin protein. *Appl. Opt.* **1997**, *36*, 1655–1659.
17 Gaigalas, A.; Gallagher, T.; Cole, K.D.; Singh, T.; Wang, L.; Zhang, Y.Z. A multistate model for the fluorescence response of R-phycoerythrin. *Photochem Photobiol.* **2006**, *82*, 635–644.
18 Guard-Friar, D.; MacColl, R.; Berns, D.S.; Wittmershaus, B.; Knox, R.S. Picosecond fluorescence of cryptomonad biliproteins. Effects of excitation intensity and the fluorescence decay times of phycocyanin 612, phycocyanin 645, and phycoerythrin 545. *Biophys. J.* **1985**, *47*, 787–793.
19 Brody, S.S. Fluorescence lifetime, yield, energy transfer and spectrum in photosynthesis, 1950-1960. *Photosynth. Res*. **2002**, *73*, 127–132.
20 Kronick, M.N.; Grossman, P.D. Immunoassay techniques with fluorescent phycobiliprotein conjugates. *Clin. Chem.* **1983**, *29*, 1582–1586.
21 Trinquet, E.; Maurin, F.; Préaudat, M.; Mathis, G. Allophycocyanin 1 as a near-infrared fluorescent tracer: isolation, characterization, chemical modification, and use in a homogeneous fluorescence resonance energy transfer system. *Anal. Biochem.* **2001**, *296*, 232–244.
22 Lakowicz, J.R. *Principles of Fluorescence Spectroscopy.* Springer; New York, **2006**.
23 Moraes, C.C.; Kalil, S.J. Strategy for a protein purification design using C-phycocyanin extract. *Bioresour. Technol*. **2009**, *100*, 5312-5317.

24 Sonani, R.R.; Singh, N.K.; Kumar, J.; Thakar, D.; Madamwar, D. Concurrent purification and antioxidant activity of phycobiliproteins from *Lyngbya* sp. A09DM: An antioxidant and anti-aging potential of phycoerythrin in *Caenorhabditis elegans*. *Process. Biochem*. **2014**, *49*, 1757-1766.
25 MacColl, R. Cyanobacterial phycobilisomes. *J. Struct. Biol*. **1998**, *124*, 311–334.
26 Glazer, A.N.; Wedemayer, G.J. Cryptomonad biliproteins-an evolutionary perspective. *Photosynth. Res*. **1995**, *46*, 93-105.
27 Troxler, R.F.; Ehrhardt, M.M.; Brown-Mason, A.S.; Offner, G.D. Primary structure of phycocyanin from the unicellular rhodophyte *Cyanidium caldarium*. II. Complete amino acid sequence of the b subunit. *J. Biol. Chem*. **1981**, *256*, 12176–12184.
28 Stec, B.; Troxler, R.F.; Teeter, M.M. Crystal structure of C-phycocyanin from *Cyanidium caldarium* provides a new perspective in phycobilisome assembly. *Biophys. J.* **1999**, 76, 2912–2921.
29 Adir, N.; Dobrovetsky, Y.; Lerner, N. Structure of C-phycocyanin from thermophilic cyanobacterium *Synechococcus vulcanus* at 2.5 Å: structural implications for thermal stability in phycobilisome assembly. *J. Mol. Biol*. **2001**, *313*, 71–81.
30 Contreras-Martel, C.; Matamala, A.; Bruna, C.; Poo-Caamaño, G.; Almonacid, D.; Figueroa, M.; Martínez-Oyanedel, J.; Bunster, M. The structure at 2 Å resolution of phycocyanin from *Gracilaria chilensis* and the energy transfer network in a PC–PC complex. *Biophys. Chem*. **2007**, *125*, 388–396.
31 Schirmer, T.D.; Bode, W.; Huber, R.; Sidler, W.; Zuber, H. X-ray crystallographic structure of the light-harvesting biliprotein C-phycocyanin from thermophilic cyanobacterium *Mastigocladus laminosus* and its resemblance to globin structures. *J. Mol. Biol*. **1985**, *184*, 257-277.
32 Adir, N.; Vainer, R.; Lerner, N. Refined structure of c-phycocyanin from the cyanobacterium *Synechococcus vulcanus* at 1.6 Å: insights into the role of solvent molecules in thermal stability and co-factor structure. *Biochim. Biophys. Acta*. **2002**, *1556*, 168-174.
33 Nield, J.; Rizkallah, P.J.; Barber, J.; Chayen, N.E. The 1.45Å three-dimensional structure of C-phycocyanin from the thermophilic cyanobacterium *Synechococcus elongates*, *J. Struct. Biol.* **2003**, *141*, 149-155.
34 Padyana, A.K.; Bhat, V.B.; Madyastha, K.M.; Rajashankar, K.R.; Ramakumar, S. Crystal structure of a light-harvesting protein C-phycocyanin from *Spirulina platensis*. *Biochem. Biophys. Res. Commun*. **2001**, *282*, 893–898.
35 Duerring, M.; Schmidt, G.B.; Huber, R. Isolation, crystallization, crystal structure analysis and refinement of constitutive C-phycocyanin from the chromatically adapting cyanobacterium *Fremyella diplosiphon* at 1.66 Å resolution. *J. Mol. Biol*. **1991**, *217*, 577–592.
36 Adir, N.; Lerner, N. The crystal structure of a novel unmethylated form of C-phycocyanin, a possible connector between cores and rods in phycobilisomes, *J. Mol. Biol*. **2003**, *278*, 25926–25932.
37 Schirmer, T.; Huber, R.; Schneider, M.; Bode, W.; Miller, M.; Hackert, M.L. Crystal structure analysis and refinement at 2.5 Å of hexameric C-phycocyanin from the cyanobacterium *Agmenellum quadruplicatum*: the molecular model and its implications for light-harvesting. *J. Mol. Biol*. **1986**, *188*, 651–676.
38 Wang, X.-Q.; Li, L.-N.; Chang, W.-R.; Zhang, J.-P.; Gui, L.-L.; Liang, D.-C. Structure of C-phycocyanin from *Spirulina platensis* at 2.2 Å resolution: a novel crystal form for phycobiliproteins in phycobilisomes. *Acta. Crystallogr*. **2001**, *D57*, 748–792.

39 Ferraro, G.; Imbimbo, P.; Marseglia, A.; Lucignano, R.; Monti, D.M.; Merlino, A. X-ray structure of C-phycocyanin from *Galdieria phlegrea*: determinants of thermostability and comparison with a C-phycocyanin in the entire phycobilisome. *Biochim. Biophys. Acta. Bioenerg*. **2020**, *1861*, 148236.
40 Gupta, G.D.; Sonani R.R.; Sharma, M.; Patel, K.; Rastogi, R.P.; Madamwar, D.; Kumar, V. Crystal structure analysis of phycocyanin from chromatically adapted *Phormidium rubidium* A09DM. *RSC. Adv.* **2016**, *6*, 77898-77907.
41 Moreno, A.; Bermejo, R.; Talavera, E.; Alvarez-Pez, J.M.; Sanz-Aparicio, J.; Romero-Garrido, A. Purification, crystallization and preliminary X-ray diffraction studies of C-phycocyanin and allophycocyanin from *Spirulina platensis*. *Acta. Crystallogr.* **1997**, *D53*, 321-326.
42 Adir, N. Elucidation of the molecular structures of components of the phycobilisome: reconstructing giant. *Photosynth. Res.* **2005**, *85*, 15-32.
43 Sarrou, I.; Feiler, C.G.; Falke, S.; Peard, N.; Yefanov, O.; Chapman, H. C-phycocyanin as a highly attractive model system in protein crystallography: unique crystallization properties and packing-diversity screening. *Acta. Crystallogr.* **2021**, *D77*, 224-236.
44 David, L.; Marx, A.; Adir, N. High-resolution crystal structures of trimeric and rod phycocyanin. *J. Mol. Biol*. **2011**, *405*, 201-213.
45 Miki, K.; Ezoe, T.; Masui, A.; Yoshisaka, T.; Mimuro, M.; Fujiwara-Arasaki, T.; Kasai, N. Crystallization and preliminary X-ray diffraction studies of C-phycocyanin from a red alga, *Porphyra tenera*. *J. Biochem*. **1990**, *108*, 646-648.
46 Scholes, G.D. Long-range resonance energy transfer in molecular systems. *Annu. Rev. Phys. Chem*. **2003**, *54*, 57-87.
47 Cunningham, F.X.; Dennenberf, R.Jr.; Jursinic, P.A.; Gantt, E. Growth under red light enhances photosystem II relative to photosystem I and phycobilisomes in the red alga *Porphyridium cruentum*. *Plant. Physiol*. **1990**, *93*, 888-895.
48 Porter, G.; Tredwell, C.J.; Searle, G.F.W.; Barber, J. Picosecond time-resolved energy transfer in *Porphyridium cruentum*. Part I, In the intact alga. *Biochim. Biophys. Acta. Bioenerg*. **1978**, *501*, 232-245.
49 Gillbro, T.; Sharkov, A.V.; Kryukov, I.V.; Khoroshilov, E.V.; Kryukov, P.G.; Fischer, R.; Scheer, H. Förster energy transfer between neighbouring chromophores in C-phycocyanin trimers. *Biochim. Biophys. Acta.* **1993**, *1140*, 321-326.
50 Xie, J.; Zhao, J.-Q.; Peng, C. Analysis of the disk-to-disk energy transfer processes in C-phycocyanin complexes by computer simulation technique. *Photosynthetica.* **2002**, *40*, 251-257.
51 Wendler, J.; John, W.; Scheer, H.; Holzwarth. A.R. Energy transfer in trimeric C-phycocyanin studied by picosecond fluorescence kinetics. *Photochem. Photobiol.* **1986**, *44*, 79-85.
52 Sandström, Å.; Gillbro, T.; Sundström, V.; Fischer, R.; Scheer, H. Picosecond time-resolved energy transfer within C-phycocyanin aggregates of *Mastigocladus laminosus*. *Biochim. Biophys. Acta.* **1988**, *933*, 42-53.
53 Sauer, K.; Scheer, H.; Sauer, P. Förster transfer calculations based on crystal structure data from *Agmenellum quadruplicatum* C-phycocyanin. *Photochem. Photobiol.* **1987**, *46*, 427-440.
54 Switalski, S.; Sauer, K. Energy transfer among the chromophores of C-phycocyanin from *Anabaena variabilis* using steady state and time-resolved fluorescence spectroscopy. *Photochem. Photobiol.* **1984**, *40*, 423-427.
55 Beck, W.F.; Sauer, K. Energy-transfer and exciton-state relaxation processes in allophycocyanin. *J. Phys. Chem*. **1985**, *96*, 4658-4666.

56 Holzwarth, A.R. Structure-function relationships and energy transfer in phycobiliprotein antennae. *Physiol. Plant.* **1991**, *83*, 518-528.
57 Gillbro, T.; Sandström, Å.; Sundström, V.; Wendler, J.; Holzwarth, A.R. Picosecond study of energy-transfer kinetics in phycobilisomes of *Synechococcus* 6301 and the mutant AN 112. *Biochim. Biophys. Acta. Bioenerg*. **1985**, *808*, 52-65.
58 Suter, G.W.; Holzwarth, A.R. A kinetic model for the energy transfer in phycobilisomes. *Biophys. J*. **1985**, *52*, 673-683.
59 Zhang, J.M.; Zhao, F.L.; Zheng, X.G.; Wang, H.Z.; Yang, T.-S.; Hayashi, M.; Lin, S.H. Excitation energy transfer processes between two trimers in C-phycocyanin hexamer from the cyanobacterium *Anabaena variabilis*. Investigation by group theory and time-resolved fluorescence spectroscopy. *J. Phtochem. Photobiol. B* **1999**, *53*, 128-135.
60 Kleima, F.J.; Hofmann, E.; Gobets, B.; van Stokkum, I.H.M.; van Grondelle, R.; Diederichs, K.; van Amerongen, H. Förster excitation energy transfer in peridinin-chlorophyll-*a*-protein. *Biophys. J.* **2000**, *78*, 344-353.
61 Demidov, A.A.; Borisov, A.Yu. Computer simulation of energy migration in the C-phycocyanin of the blue-green algae *Agmenellum quadruplicate um*. *Biophys. J.* **1993**, *64*, 1375-1384.
62 Riter, R.R.; Edington, M.D.; Beck, W.F. Protein-matrix solvation dynamics in the α subunit of C-phycocyanin. *J. Phys. Chem*. **1996**, *100*, 14198-14205.
63 Sharkov, A.V.; Krykov, I.V.; Khoroshilov, E.V.; Kryukov, P.G.; Fischer, R.; Scheer, H.; Gillbro, T. Femtosecond energy transfer between chromophores in allophycocyanin trimers. *Chem. Phys. Lett*. **1992**, *191*, 633-638.
64 Acuña, A.M.; Van Alphen, P.; Van Grondelle, R.; Van Stokkum, I.H.M. The phycobilisome terminal emitter transfers its energy with a rate of $(20\ ps)^{-1}$ to photosystem II. *Photosynthetica*. **2018**, *56*, 265-274.
65 Förster, Th. Delocalized excitation and excitation transfer. In: *Modern Chemistry Istanbul Lectures*, vol. 3 (ed. O. Sinanoglu), Academic Press, New York, pp.93-137.
66 Förster, T. Transfer mechanisms of electronic excitation energy. *Radiat. Res. Suppl*. **1960**, *2*, 326-339.
67 Müller, S.M.; Galliardt, H.; Schneider, J.; Barisas, B.G.; Seidel, T. Quantification of Förster resonance energy transfer by monitoring sensitized emission in living plant cells. *Front. Plant Sci*. **2013**, **4**, 413, 1-20.
68 Sauer, K.; Scheer, H. Excitation transfer in C-phycocyanin. Förster transfer rate and exciton calculations based on new crystal structure data for C-phycocyanins from *Agmenellum quadruplicatum* and *Mastigocladus laminosus*. *Biochim. Biophys. Acta*. **1988**, *936*, 157-170.
69 You, Z.-Q.; Hsu, C.-P. Theory and calculation for the electronic coupling in excitation energy transfer. *Int. J. Quantum Chem*. **2014**, *114*, 102-115.
70 Kimura, A.; Kakitani, T. Advanced theory of excitation energy transfer in dimers. *J. Phys. Chem. A* **2007**, *111*, 12042-12048.
71 Ma, J.; Cao, J. Förster resonance energy transfer, absorption and emission spectra in multichromophoric systems. I. Full cumulant expansions and system-bath entanglement. *J. Chem. Phys*. **2015**, *142*, 094106.
72 Scholes, G.D., Jordanides, X.J. Flemming, G.R. Adapting the Förster theory of energy transfer for modeling dynamics in aggregated molecular assemblies. *J. Phys. Chem. B* **2001**, *105*, 1640-1651.

73 Ahn, T.-S.; Wright, N.; Bardeen, C.J. The effects of orientational and energetic disorder on Förster energy migration along a one-dimensional lattice. *Chem. Phys. Lett*. **2007**, *446*, 43-48.
74 Sagvolden, S.; Furche, F.; Köhn, A. Förster energy transfer and Davydov splittings in time-dependent density functional theory: Lessons from 2-pyridone dimer, *J. Chem. Theory Comput*. **2009**, *5*, 873-880.
75 Jang, S. generalization of the Förster resonance energy transfer theory for quantum mechanical modulation of the donor-acceptor coupling, *J. Chem. Phys*. **2007**, *127*, 174710.
76 Mimuro, M.; Füglistaller, P.; Rümbeli, R.; Zuber, H. Functional assignment of chromophores and energy transfer in C phycocyanin isolated from the thermophilic cyanobacterium *Mastigocladus laminosus*. *Biochim. Biophys. Acta*. **1986**, *848*, 155-166.
77 Konrad, A.; Metzger, M.; Kern, A.M.; Brecht, M.; Controlling the dynamics of Förster resonance energy transfer inside a tunable sub-wavenlength Fabry-Pérot-resonator. *Nanoscale*. **2015**, *7*, 10204-10209.
78 Abeywickrama, C.; Premaratne, M.; Gunapala, S.D.; Andrews, D.L. Impact of a charged neighboring particle on Förster resonance energy transfer (FRET). *J. Phys. Condens. Matter*. **2020**, *32*, 095305.
79 Padyana, A.K.; Ramakumar, S. Lateral energy transfer model for adjacent light-harvesting antennae rods of C-phycocyanins. *Biochim. Biophys. Acta*. **2006**, *1757*, 161-165.
80 Debreczeny, M.P.; Sauer, K.; Zhou, J.; Bryant, D.A. Comparison of calculated and experimentally resolved rate constants for excitation energy transfer in C-phycocyanin. 1. Monomers. *J. Phys. Chem.* **1995**, *99*, 8412-8419.
81 Figueroa, M.; Martínez-Oyanedel, J.; Matamala, A.R.; Dagino-Leone, J.; Mella, S.; Fritz, R.; Sepúlveda-Ugarte, J.; Bunster, M. *In silico* model of an antenna of a phycobilisomes and energy transfer rates determination by theoretical Förster approach. *Protein. Sci*. **2012**, *21*, 1921-1928.
82 Ren, Y.; Chi, B.; Melhem, O.; Wei, K.; Feng, L.; Li, Y.; Han, X.; Li, D.; Zhang, Y.; Wan, J.; Xu, X.; Yang, M. Understanding the electronic energy transfer pathways in the trimeric and hexameric aggregation state of Cyanobacteria Phycocyanin within the framework of Förster theory. *J. Comput. Chem*. **2013**, *34*, 1005-1012.
83 Ren, Y.; Melhem, O.; Li, Y.; Chi, B.; Han, X.; Zhu, H.; Feng, L.; Wan, J.; Xu, X. Clarifying and illustrating the electronic energy transfer pathways in trimeric and hexameric aggregation state of Cyanobacteria allophycocyanin within the framework of Förster theory. *J. Comput. Chem*. **2015**, *36*, 137-145.
84 The molecular biology of cyanobacteria, ed. Bryant, D.A. (Dordrecht: Kluwer Academic Publishers).
85 Algal green chemistry Recent progress in biotechnology, Rastogi, R.P.; Madamwar, D.; Pandey, A. (Amsterdam: Elsevier), **2017**.
86 Eriksen, N.T. Production of phycocyanin-a pigment with applications in biology, biotechnology, foods, and medicine. *Appl. Microbiol. Biotechnol*. **2008**, *80*, 1-14.
87 Squires, A.H.; Moerner, W.E. Direct single-molecule measurements of phycocyanobilin photophysics in monomeric C-phycocyanin. *Proc. Natl. Acad. Sci. USA*. **2017**, *114*, 9779-9784.
88 Gaussian 16, Revision B.01, Frisch, M. J.; Trucks, G. W.; Schlegel, H. B.; Scuseria, G. E.; Robb, M. A.; Cheeseman, J. R.; Scalmani, G.; Barone, V.; Petersson, G. A.; Nakatsuji, H.; Li, X.; Caricato, M.; Marenich, A. V.; Bloino, J.; Janesko, B. G.; Gomperts, R.; Mennucci, B.; Hratchian, H. P.; Ortiz, J. V.; Izmaylov, A. F.; Sonnenberg, J. L.; Williams-Young, D.; Ding, F.; Lipparini, F.; Egidi, F.; Goings, J.; Peng, B.; Petrone, A.; Henderson, T.; Ranasinghe, D.; Zakrzewski, V. G.; Gao, J.; Rega, N.; Zheng, G.; Liang, W.; Hada, M.; Ehara, M.; Toyota, K.;

Fukuda, R.; Hasegawa, J.; Ishida, M.; Nakajima, T.; Honda, Y.; Kitao, O.; Nakai, H.; Vreven, T.; Throssell, K.; Montgomery, J. A., Jr.; Peralta, J. E.; Ogliaro, F.; Bearpark, M. J.; Heyd, J. J.; Brothers, E. N.; Kudin, K. N.; Staroverov, V. N.; Keith, T. A.; Kobayashi, R.; Normand, J.; Raghavachari, K.; Rendell, A. P.; Burant, J. C.; Iyengar, S. S.; Tomasi, J.; Cossi, M.; Millam, J. M.; Klene, M.; Adamo, C.; Cammi, R.; Ochterski, J. W.; Martin, R. L.; Morokuma, K.; Farkas, O.; Foresman, J. B.; Fox, D. J. Gaussian, Inc., Wallingford CT, **2016**.

89 Runge, E.; Gross, E. K. U. Density functional theory for time-dependent systems. *Phys. Rev. Lett*. **1984**, *52*, 997-1000.

90 Furche, F.; Ahlrichs, R. Adiabatic time-dependent density functional methods for excited state properties. *J. Chem, Phys*. **2002**, *117*, 7433-7447.

91 Becke, A.D. A new mixing of Hartree-Fock and local density-functional theories, J. Chem. Phys. **1993**, *98*, 1372.

92 Tomasi, J.; Mennucci,B.;Cammi,R. Quantum mechanical continuum solvation models. *Chem, Rev*. **2005**, *105*, 2999-3093.

93 Wan, J.; Xu, X.; Ren, Y.; Yang, G. A time dependent density functional theory study of α-84 Phycocyanobilin chromophore in C-Phycocyanin, *J. Phys. Chem. B* **2005**, *109*, 11088-11090.

94 Ren, Y.; Wan, J.; Xu, X.; Zhang, Q.; Yang, G. A time-dependent density functional theory investigation of the spectroscopic properties of the β-subunit of C-Phycocyanin, *J. Phys. Chem. B* **2006**, *110*, 18665-18669.

95 Borg, O. A.; Durbeej, B. Relative ground and excited-state pKa values of phytochromobilin in the photoactivation of phytochrome: A computational study. *J. Phys. Chem. B* **2007**, *111*, 11554-11565.

96 Blomberg, M. R. A.; Siegbahn, P E.M.; Babcock, G. T. Modeling electron transfer in biochemistry: A quantum chemical study of charge separation in *Rhodobacter sphaeroides* and photosystem II. *J. Am. Chem, Soc*. **1998**, *120*, 8812-8824.

97 GaussView, Version 6.1, Roy Dennington, Todd A. Keith, and John M. Millam, Semichem Inc., Shawnee Mission, KS, **201**

98 Curutchet, C., R.; Scholes, G.D.; Mennucci, B.; Cammi, R. How solvent controls electronic energy transfer and light harvesting: Toward a quantum-mechanical description of reaction field and screening effects. *J. Phys. Chem. B* **2007**, *111*, 13253-13265.

99 Ren, Y.; Chi, B.; Melhem, O.; Wei, K.; Feng, L.; Li, Y.; Han, X.; Li, D.; Zhang, Y.; Wan, J.; Xu, X.; Yang, M. Understanding the electronic energy transfer pathways in the trimeric and hexameric aggregation state of Cyanobacteria Phycocyanin within the framework of Förster theory. *J. Comput. Chem*. **2013**, *34*, 1005-1012.

100 Matute, R.A.; Contreras, R.; Pérez-Hernández, G.; González, L. The chromophore structure of the cyanobacterial phytochrome Cph1 as predicted by time-dependent density functional theory. *J. Phys. Chem. B Lett*. **2008**, *112*, 16253-16256.

101 Sundström, V.; Pullerits, T.; van Grondelle, R. Photosynthetic light-harvesting: reconciling dynamics and structure of purple bacterial LH2 reveals function of photosynthetic unit. *J. Phys. Chem. B* **1999**, *103*, 2327-2346.

102 Tian, L.; Feiwu, C. Multiwfn: a multifunctional wavefunction analyzer. *J. Compt. Chem*., **2012**, *33*, 580-592.

103 Beljonne, D.; Curutchet, C.; Scholes, G.D.; Silbey, R.J. Beyond resonance Förster resonance energy transfer in biological and nanoscale systems. *J. Phys. Chem. B* **2009**, *113*, 6583-6599.

104 Blumberger, J. Recent advances in the theory and molecular simulation of biological electron transfer reactions. *Chem. Rev.* **2015**, *115*, 11191-11238.
105 Mancini, J.A.; Sheehan, M.; Kodali, G.; Chow, B.Y.; Bryant, D.A.; Dutton, P.L.; Moser, C.C. De novo synthetic biliprotein design, assembly and excitation energy transfer, *J. R. Soc.Interface*, **2018**, *15*, 20180021.
106 Mishima, K.; Shoji, M.; Umena, Y.; Boero, M.; Shigeta, Y. Role of propionic acid side-chain of C-Phycocyanin chromophores in the excited states for the photosynthesis process. *Bull. Chem. Soc. Japan*. **2020**, *93*, 1509-1519.
107 Zienicke, B.; Molina, I.; Glenz, R.; Singer, P.; Ehmer, D.; Escobar, F.V.; Hildebrandt, P.; Diller, R.; Lamparter, T. Unusual spectral properties of bacteriophytochrome Agp2 result from a deprotonation of chromophore in the red-absorbing form Pr*. *J. Biol.Chem*. **2013**, *288*, 31738-31751.
108 Stillman, H.J. in Handbook of Porphyrin Science, World Scientific Publishing, Singapore, **2011**, vol. 14, ch. 65, pp. 461–524.
109 Gouterman, M., in The Porphyrins, ed. D. Dolphin, Academic Press, New York, **1978**, vol. 3, ch. 1, pp. 1–165.